



Disk or Companion: Characterizing Excess Infrared Flux in Seven White Dwarf Systems with Near-infrared Spectroscopy

Dylan Owens¹ , Siyi Xu (许偲艺)¹ , Elena Manjavacas^{2,3} , S. K. Leggett¹ , S. L. Casewell⁴ , Erik Dennihy⁵ , Patrick Dufour^{6,7} , Beth L. Klein⁸ , Sherry Yeh⁹ , and B. Zuckerman⁸

¹ Gemini Observatory/NSF's NOIRLab, 670 N. A'ohoku Place, Hilo, Hawaii, 96720, USA; dylowens6@gmail.com

² AURA for the European Space Agency (ESA), ESA Office, Space Telescope Science Institute, 3700 San Martin Drive, Baltimore, MD 21218 USA

³ Department of Physics and Astronomy, Johns Hopkins University, Baltimore, MD 21218, USA

⁴ School of Physics and Astronomy, University of Leicester, University Road, Leicester LE1 7RH, UK

⁵ Rubin Observatory Project Office, 950 N. Cherry Avenue, Tucson, AZ 85719, USA

⁶ Institut de Recherche sur les Exoplanètes (iREx), Université de Montréal, Montréal, QC H3C 3J7, Canada

⁷ Département de physique, Université de Montréal, Montréal, QC H3C 3J7, Canada

⁸ Department of Physics and Astronomy, University of California, Los Angeles, CA 90095-1562, USA

⁹ W.M. Keck Observatory, 65-1120 Mamalahoa Hwy. Kamuela, HI, USA

Received 2022 December 23; revised 2023 March 20; accepted 2023 March 21; published 2023 June 6

Abstract

Excess infrared flux from white dwarf stars is likely to arise from a dusty debris disk or a cool companion. In this work, we present near-infrared spectroscopic observations with Keck/MOSFIRE, Gemini/GNIRS, and Gemini/Flamingos-2 of seven white dwarfs with infrared excesses identified in previous studies. We confirmed the presence of dust disks around four white dwarfs (Gaia J0611–6931, Gaia J0006+2858, Gaia J2100+2122, and WD 0145+234) as well as two new white dwarf–brown dwarf pairs (Gaia J0052+4505 and Gaia J0603+4518). In three of the dust disk systems, we detected for the first time near-infrared metal emissions (Mg I, Si I, and possibly Fe I) from a gaseous component of the disk. We developed a new Markov Chain Monte Carlo framework to constrain the geometric properties of each dust disk. In three systems, the dust disk and the gas disk appear to coincide spatially. For the two brown dwarf–white dwarf pairs, we identified broad molecular absorption features typically seen in L dwarfs. The origin of the infrared excess around Gaia J0723+6301 remains a mystery. Our study underlines how near-infrared spectroscopy can be used to determine sources of infrared excess around white dwarfs, which has now been detected photometrically in hundreds of systems.

Unified Astronomy Thesaurus concepts: [Infrared spectroscopy \(2285\)](#); [Infrared excess \(788\)](#); [Brown dwarfs \(185\)](#); [White dwarf stars \(1799\)](#); [Debris disks \(363\)](#)

Supporting material: data behind figure

1. Introduction

The vast majority of stars within the Galaxy will one day reach the last stage of their evolution as white dwarfs. Some main-sequence stars are in binary systems with substellar companions—which can be difficult to detect and characterize, given the much brighter primary. When the primary reaches the white dwarf stage, it becomes an excellent target to search for low-mass companions. Because hot white dwarfs emit mostly at ultraviolet and optical wavelengths, cooler sources of emission can be detected as excess flux in the infrared. Even a small infrared excess can be detected in the Spectral Energy Distributions (SEDs) of a white dwarf (Steele et al. 2011).

White dwarfs with debris disks, on the other hand, offer unique insight into the composition of the exoplanetary bodies that orbited the progenitor star. These bodies can be perturbed to pass within the tidal radius of the white dwarf, which disrupts them to form a dusty disk (Jura 2003; Veras et al. 2014). Analysis of such systems offers the opportunity to constrain the composition of exoplanetary material (e.g., Klein et al. 2010), as well as to better understand the dynamics of the last stage of evolution of planetary systems (Xu & Jura 2014;

Wang et al. 2019). Some dusty white dwarfs also exhibit a gaseous component, which often appears as double-peaked emission features (Gänsicke et al. 2006; Manser et al. 2020).

About a dozen unresolved white dwarf–brown dwarf pairs are currently known, and their evolutionary path is of great interest (Casewell et al. 2020). If the brown dwarf was originally within ≈ 5 au of the white dwarf progenitor, it would likely have been engulfed during its red giant phase, causing the brown dwarf to spiral inward to its current, likely tidally locked position (Lagos et al. 2021). The close orbits of such white dwarf–brown dwarf pairs cause the brown dwarf to be irradiated on one hemisphere, similarly to hot Jupiters. Thus, they are great analogs for studying the irradiated atmospheres of hot Jupiters orbiting main-sequence stars, yet much easier to observe, given the faintness of white dwarfs at infrared wavelengths (Zhang et al. 2017; Lew et al. 2021). These extreme atmospheric environments and evolutionary paths also present an interesting comparison with their much better-understood field brown dwarf counterparts. If the brown dwarf was more widely separated from the white dwarf progenitor, they would have evolved like two single stars. There are about a dozen wide white dwarf–brown dwarf pairs, which were detected via direct imaging (e.g., Becklin & Zuckerman 1988; French et al. 2023). Sometimes, the evolution path is less clear, as in the case of the recent discovery of Gaia 0007-1605, an old hierarchical triple system with an inner white dwarf–brown

Table 1
White Dwarf Parameters

Name	R.A. (deg)	decl. (deg)	Distance (pc)	SpT	T_{eff} (K)	$\log g$ (cm s^{-2})	$\log n(\text{Ca})/n(\text{H})$	\dot{M}_{Ca} (g s^{-1})	Reference
Gaia J0006+2858	1.644755	28.979655	151.95 ± 1.75	DAZ	23921 ± 335	8.04 ± 0.04	-6.17 ± 0.10	7.9×10^6	Rogers (2023)
Gaia J0052+4505	13.018295	45.092722	75.28 ± 0.25	DA	12858 ± 77	7.97 ± 0.01	$< -8.8^{\text{a}}$	$< 1.6 \times 10^4$	Kilic et al. (2020)
WD 0145+234	26.978382	23.661678	29.43 ± 0.02	DAZ	12720 ± 1000	8.1 ± 0.1	-6.6 ± 0.2	4.3×10^6	Melis et al. (2020)
Gaia J0603+4518	90.786320	45.307719	60.30 ± 0.12	DA	16177 ± 323	8.00 ± 0.03	$< -8.3^{\text{a}}$	$< 3.8 \times 10^4$	Gentile Fusillo et al. (2021)
Gaia J0611-6931	92.882367	-69.516818	143.13 ± 1.05	DAZ	17749 ± 248	8.14 ± 0.04	-6.03 ± 0.19	8.2×10^6	Rogers (2023)
Gaia J0723+6301	110.823019	63.024055	137.90 ± 1.12	DA	18488 ± 654	7.92 ± 0.05	$< -7.0^{\text{a}}$	$< 7.5 \times 10^5$	Gentile Fusillo et al. (2021)
Gaia J2100+2122	315.144721	21.382640	88.08 ± 0.36	DAZ	25565 ± 358	8.10 ± 0.04	-6.22 ± 0.14	8.0×10^6	Rogers (2023)

Note. Coordinates and distances are from Gaia DR3 (Gaia Collaboration et al. 2022).

^a New analysis from this paper.

Table 2
Observing Log

Name	UT Date	Instrument	Wavelength (μm)	Exposure Time	Resolution	S/N	Telluric	Telluric T_{eff} (K)
GaiaJ0006+2858	10-09-2020	MOSFIRE	1.16–2.40	J, H: 120 s \times 4; K: 180 s \times 4	2200	19	HIP 1123	9579
GaiaJ0052+4505	10-09-2020	MOSFIRE	1.16–2.40	J, H: 120 s \times 4; K: 180 s \times 4	2200	22	HIP 13121	9620
WD 0145+234	10-09-2020	MOSFIRE	1.16–2.40	J, H: 120 s \times 4; K: 180 s \times 4	2200	53	HIP 13121	9620
GaiaJ0603+4518	10-09-2020	MOSFIRE	1.49–2.40	H: 60 s \times 4; K: 180 s \times 4	2200	20	HIP 13121	9620
	12-12-2021	GNIRS	0.843–2.53	180 s \times 12	660	24	HD 26603	11795
GaiaJ0611–6931	12-24-2022	Flamingos-2	0.703–2.65	JH: 100s \times 24, HK: 100 s \times 20	750	42	HD 69784	9020
GaiaJ0723+6301	02-07-2022	GNIRS	0.827–2.53	300 s \times 16	540	7	HD 63312	8475
GaiaJ2100+2122	10-09-2020	MOSFIRE	1.16–2.40	J, H: 120 s \times 4; K: 180 s \times 4	2200	41	HIP 1123	9579
GaiaJ0052+4505	09-22-2019	HIRESb	0.32–0.59	2100 s \times 2	40,000	12
GaiaJ0603+4518	12-05-2019	HIRESb	0.32–0.59	1200 s+1100 s	40,000	45
GaiaJ0723+6301	12-05-2019	HIRESb	0.32–0.59	1800 s \times 2	40,000	15

Notes. Resolution is measured directly on the final spectra. S/N is estimated in regions without emission/absorption features between 1.5 and 1.7 μm for the infrared data and around Ca II 3933 Å in the optical data. The telluric standard effective temperatures are from Anders et al. (2022).

dwarf binary and an outer white dwarf system (Rebassa-Mansergas et al. 2022).

There is much to be learned from the analysis of both white dwarf systems with debris disks as well as systems with substellar companions. While many infrared-excess candidate systems have been identified with photometry, differentiating between the two possible sources of excess flux can be challenging (Xu et al. 2020). Lai et al. (2021) and Barber et al. (2014) outlined one method for disentangling the two possible scenarios using *J*-band photometry. Since the dust sublimation temperatures of dust disks are around 2500 K (Rafikov & Garmilla 2012), they are not expected to show significant excess at wavelengths shorter than 2 μm . Low-mass companions, in comparison, can span a much larger range of temperatures and have been shown to result in a significant *J*-band excess. Thus, the detection of significant *J*-band excess can rule out a dust disk in favor of a low-mass companion. However, this method is limited, as a lack of *J*-band excess does not necessarily confirm a dust disk over a companion. Near-infrared spectroscopy is a much more effective method of determining the source of excess in a white dwarf system.

In this paper, we present new infrared spectroscopic observations of seven infrared-excess white dwarfs listed in Table 1. They were initially identified as infrared excess candidates by cross-correlating Gaia DR2 and the unWISE catalog (Xu et al. 2020) and followed up with the Spitzer Space Telescope (Lai et al. 2021). Four of the systems, GaiaJ0006+2858, WD 0145+234, Gaia J0611–6931, and GaiaJ2100+2122, were shown to have metals in their photospheres as well as circumstellar gas emissions (Dennihey et al. 2020; Melis et al. 2020). Two other systems, GaiaJ0052+4505 and Gaia J0603+4518, show excess in their *J*-band photometry.

In Section 2, we describe the methods used to collect the spectroscopic data with Keck/MOSFIRE, Gemini/GNIRS, Flamingos-2, and Keck/HIRES, along with the data reduction steps. In Sections 3 and 4, we describe our methods of analysis, which include identifying spectral features and fitting the spectroscopic data. In Section 5, we summarize the analysis of each individual system and give the most likely source of the infrared excess for each. In Section 6, we conclude by outlining our results as well as the next steps forward for better understanding these and other white dwarfs with infrared excess.

2. Observation and Data Reduction

2.1. Near-infrared Spectroscopy from Keck/MOSFIRE

We used the MOSFIRE multi-object near-infrared spectrograph (McLean et al. 2010, 2012), installed at the Keck I telescope to observe Gaia J0006+2858, GaiaJ0052+4505, WD 0145+4505, Gaia J0603+4518, and GaiaJ2100+2122. In Table 2, we show the details of the observations. We used MOSFIRE in a long slit (1''0 slit width) configuration. A single photometric band is covered in each instrument setting (*J*, *H*, or *K*). We observed all the targets, as well as the telluric standards HIP 1123 (A1 spectral type) and HIP 13121 (A0 spectral type), with a 1''5 ABBA pattern.

We used version 1.7.1 of PypeIt¹⁰ to reduce all the spectra (Prochaska et al. 2019, 2020). The pipeline corrected the raw images for dark current and generated a bad-pixel mask. The edges of the slits were traced using dome flats, and a master flat was also created. PypeIt produced a wavelength calibration via use of the sky lines present in the 2D spectra. The wavelength calibration accounted for the spectral tilt across the slit. The calibrations were applied to our science frames, and the sky was subtracted using the A-B or B-A frames following Kelson (2003). The 1D science spectra were extracted from the 2D sky-corrected frames. All the white dwarfs appear as single objects in the acquisition images. We measured the Full Width at Half Maximum (FWHM) in the 2D science spectra to be 0''7.

Telluric correction was performed using the spectra of the corresponding telluric standard stars, as listed in Table 2. Hydrogen and helium features from each telluric standard's spectrum were removed individually by dividing them by a Gaussian-smoothed version of the spectrum in that region. This process removed the standard star's stellar features while preserving the telluric lines. The spectra of each telluric standard star were also divided by a blackbody curve at the star's effective temperature, leaving only telluric lines in their spectra. Telluric-corrected target spectra were flux calibrated with the near-infrared photometry reported in Lai et al. (2021). Figure 1 shows the final calibrated spectra for each system.

¹⁰ <https://github.com/pypeit/PypeIt>

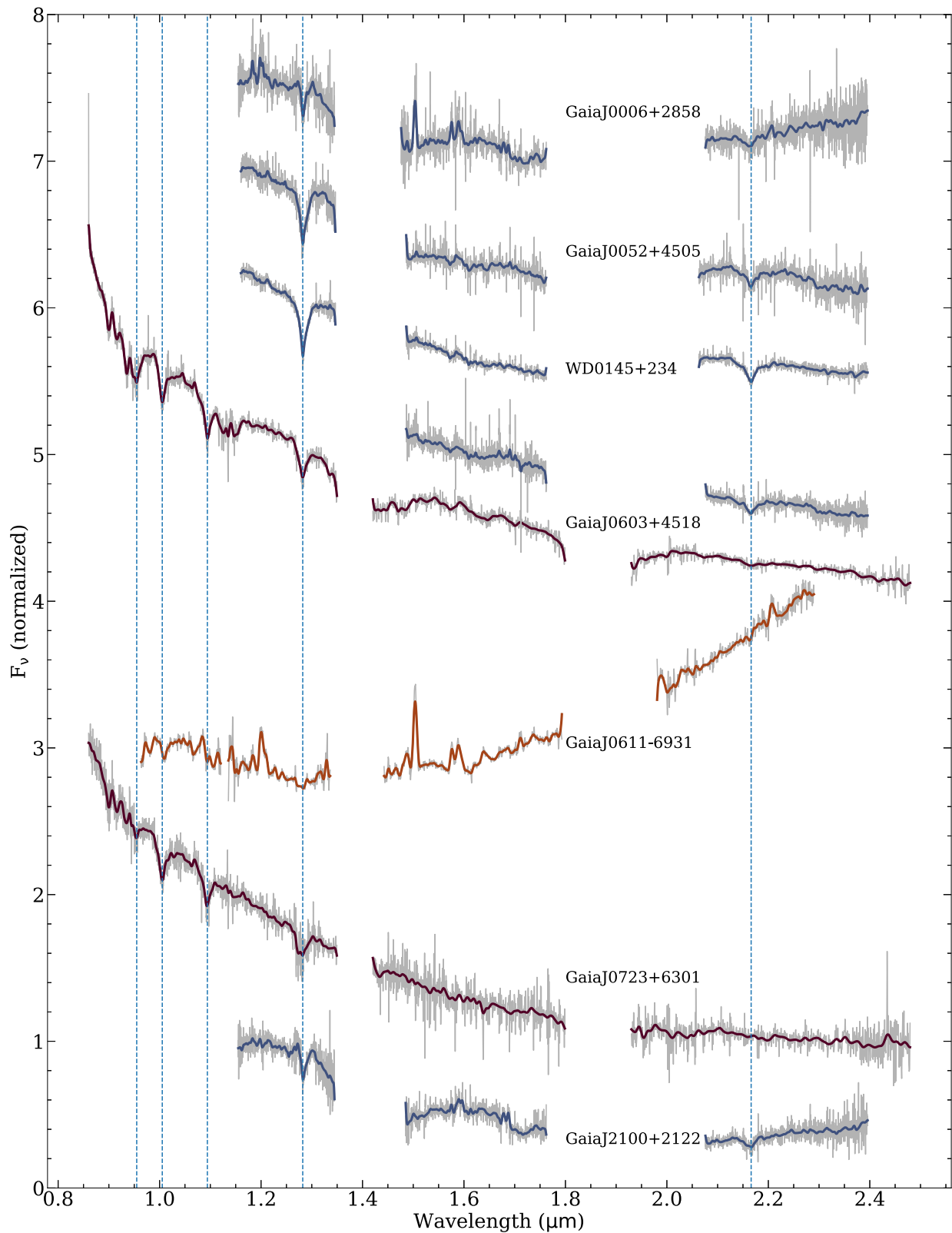


Figure 1. Flamingos-2 (orange), MOSFIRE (dark blue), and GNIRS (brown) spectra for each system. Spectra are divided by their median flux value, are offset by a constant from each other, and are smoothed by a Gaussian filter with a standard deviation of 3 (Flamingos-2), 10 (MOSFIRE), or 7 (GNIRS) pixels, respectively. White dwarf hydrogen line centroids are identified by blue dashed lines: 0.955 μm Paschen 8, 1.005 μm Paschen 7, 1.094 μm Paschen 6, 1.282 μm Paschen 5, and 2.166 μm Brackett 7. Additional emission and absorption features are detected in most white dwarfs (see Section 3 for further discussion). The data behind this figure are published in machine-readable format.

(The data used to create this figure are available.)

2.2. Near-infrared Spectroscopy from Gemini-N/GNIRS

Gaia J0603+4518 and Gaia J0723+6301 were observed with Gemini/GNIRS (Elias et al. 2006) via the program GN-2021B-Q-325. The short blue camera was used with the 321/mm grating in the cross-dispersed mode, which provides a continuous wavelength coverage of 0.8–2.5 μm . We used a 1''0 wide slit. The standard ABBA nod pattern was adopted to facilitate sky subtraction. The exposure times are listed in Table 2. Telluric standards were observed with the same configuration immediately before/after the science observations. Data reduction was performed using PyPeIt (Prochaska et al. 2019, 2020) and custom scripts, similarly to the MOSFIRE data reduction procedure. In the acquisition images in *H* band, both Gaia J0603+4518 and Gaia J0723+6301 appear as one single object, with a FWHM around 1''0.

2.3. Near-infrared Spectroscopy from Gemini-S/Flamingos-2

Gemini/Flamingos-2 (Eikenberry et al. 2004) was used to observe Gaia J0611–6931 via the program GS-2021B-Q-244. We used a long slit 3 pixels (0''54) wide with both the *JH* and *HK* grisms, which provides a complete wavelength coverage of 0.7–2.5 μm . The sky was clear and seeing was 0''7. The observing log is shown in Table 2. The telluric standard HD 69784 was observed immediately after the science observations. Data reduction was performed using PyPeIt, similarly to the MOSFIRE and GNIRS observations. In the acquisition image in *H* band, Gaia J0611–6931 is an isolated object with a FWHM of 0''7.

2.4. Optical Spectroscopy from Keck/HIRES

Gaia J0052+4505, Gaia J0603+4518, and Gaia J0723+6301 were observed in 2019 with the High Resolution Echelle Spectrometer (HIRES) on the Keck I Telescope (Vogt et al. 1994) via program 2019B_N072, as part of our effort to characterize Gaia white dwarfs with infrared excess. The observing log is in Table 2 and clouds were variable during the night. Data reduction was performed using the MAKEE package and then continuum normalized with IRAF, following our previous HIRES observations (Xu et al. 2016). In all three stars, we identified broad Balmer lines from the white dwarf, and their radial velocities are consistent to within $\approx 30 \text{ km s}^{-1}$ in the consecutive spectra. We did not find any narrow absorption features from heavy elements or narrow emissions from potential companions. We focused on the Ca II-K line around 3933 Å and followed procedures described in Rogers (2023). An upper limit in the equivalent width (EW) of Ca II K line was derived, which is 32, 10, and 28 mÅ for Gaia J0052+4518, Gaia J0603+4505, and Gaia J0723+6301, respectively. We then computed white dwarf model atmospheres (Dufour et al. 2007) and derived an upper limit on the calcium abundance and mass accretion rate, as shown in Figure 2 and Table 1.

The remaining four white dwarfs, i.e., Gaia J0006+2858, WD 0145+234, Gaia J0611–6931, and Gaia J2100+2122, are heavily polluted, and the abundance analysis has been reported in Rogers (2023; see Table 1).

3. Spectral Feature Analysis

In hot DA (hydrogen-dominated) white dwarfs, like those in this sample, there are only a few hydrogen lines from the star's

atmosphere in the spectra, making features from a disk or companion easily detectable. The infrared spectra of debris disks and brown dwarf companions have different characteristics, which can be used to assess the source of infrared excess. Previous near-infrared observations of white dwarfs with debris disks show that these systems have a featureless continuum from heated dust (Kilic et al. 2008; Melis et al. 2011). Mid-infrared studies using the Spitzer/IRS have detected broad silicate emissions centered at 10 μm , which have been modeled to originate from an optically thin region of a dust disk (Reach et al. 2005; Jura et al. 2007). On the other hand, for white dwarf–brown dwarf pairs, we expect to see broad absorption bands from molecules in the brown dwarf's atmosphere (McLean et al. 2003; Casewell et al. 2020; Lew et al. 2021). In the infrared, prominent absorption features come from H₂O in the *J* band, and CO in the *K* band (McLean et al. 2003).

In all the systems, with the exception of Gaia J0611–6931, we have detected broad hydrogen absorption lines from the photosphere of each white dwarf, as shown in Figure 1. These lines were consistent with our white dwarf models (Dufour et al. 2007) calculated from the T_{eff} and $\log g$ for each system. It is interesting that we did not detect Paschen or Brackett lines in Gaia J0611–6931, even though the Balmer series are clearly detected and well modeled in the optical data (Rogers 2023). Gaia J0611–6931 shows strong emission features (see Section 5.5) throughout the near-infrared, and we suspect there are additional emission features around the Paschen and Brackett lines, complicating their detections.

3.1. Gaseous Debris Emissions

For the first time, we detected strong infrared emission features in Gaia J0006+2858, Gaia J0611–6931, and Gaia J2100+2122, as shown in Figure 3. These three systems also host a range of metal emissions in their optical spectra, such as Ca II, O I, Fe II, Mg I, Si I, and Na I (Dennihy et al. 2020; Melis et al. 2020). We used the optical line identifications and transition properties to help with our own line identification of the infrared emission lines. We used atomic line lists from Van Hoof (2018)¹¹ to query transition properties (transition energy levels, Einstein coefficients, and oscillator strengths). Comparing transition characteristics from lines identified in previous studies, we tried to find the most likely candidate for each observed feature. As an additional confirmation, we checked if there were other lines of the same element that we would also expect to see, given the properties of the candidate transition. If there were other expected transitions within the wavelength range of our data that we did not observe, then we rejected that candidate. Due to the lower resolution of the infrared spectra, the emission features appear as one broad single peak, as opposed to the double-peaked features in the optical observations (Dennihy et al. 2020; Melis et al. 2020). We fit each observed line with a Gaussian function to determine the feature's centroid. We calculated line properties including the full width at zero intensity (FWZI), equivalent width (EW), and radial velocity (RV). Table 3 reports the properties of the emission features that we identified for each system.

In Gaia J0006+2858, Gaia J0611–6931, and Gaia J2100+2122, we identified emission features consistent with the species observed in previous optical studies including Mg I, Si

¹¹ <https://www.pa.uky.edu/~peter/newpage/>

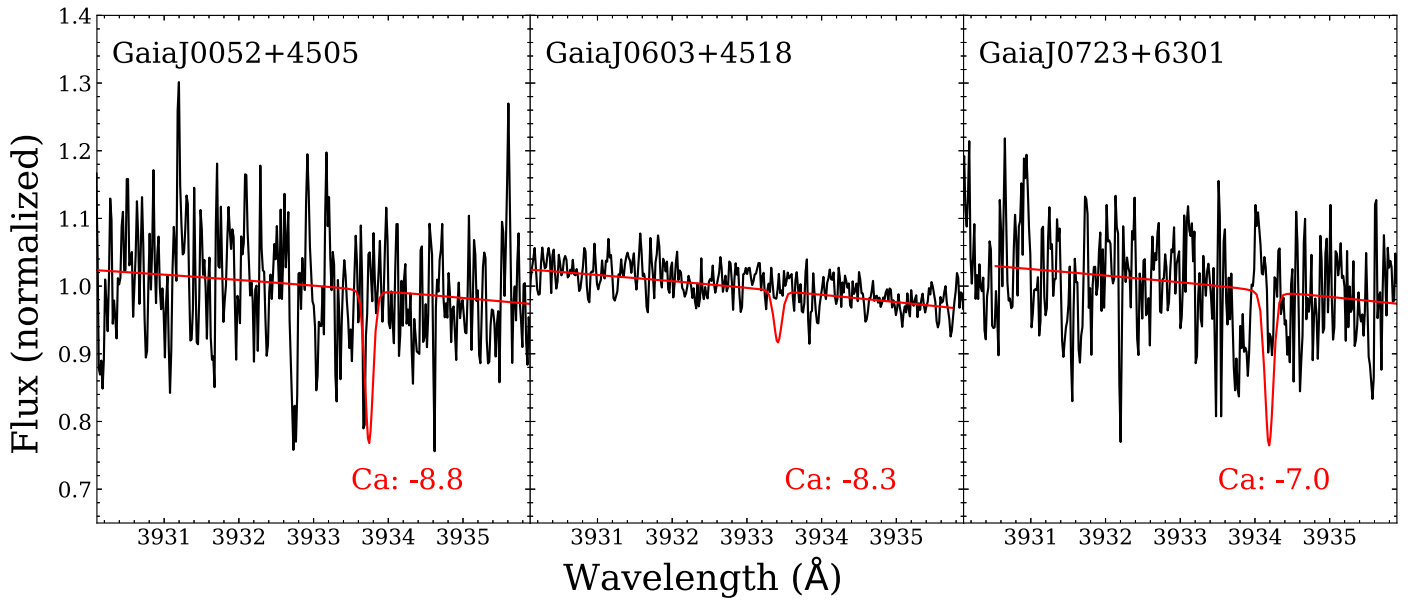


Figure 2. Keck/HIRES observations around the Ca II K line region for Gaia J0052+4505, Gaia J0603+4518, and Gaia J0723+6301. The red lines are the white dwarf model that incorporates some amount of Ca, whose abundance is listed in each panel. Calcium is not detected in these systems, and the abundances are upper limits. The model spectra has been shifted to match the radial velocities of each white dwarf (measured from the Balmer lines).

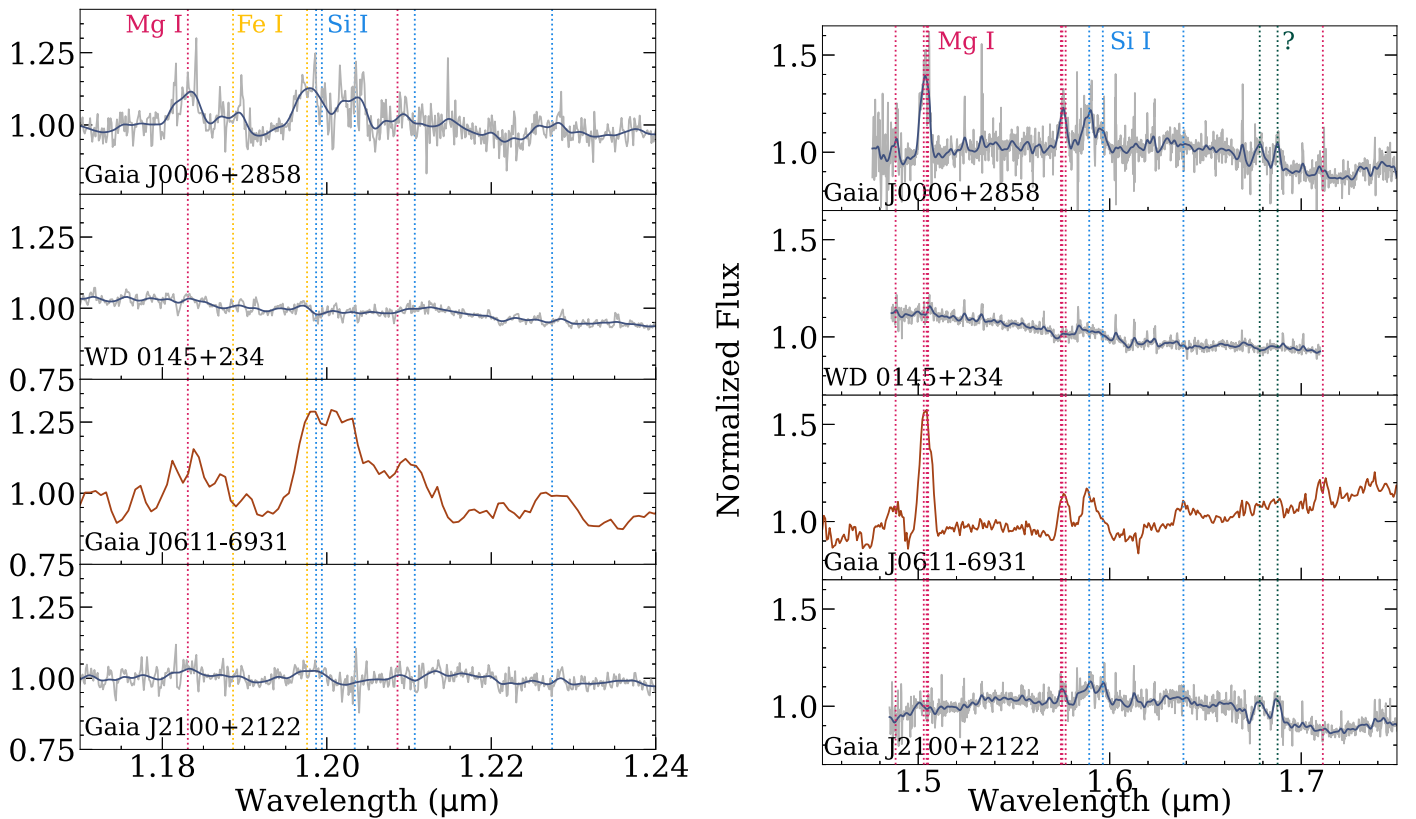


Figure 3. Spectra of near-infrared emission lines for each of the disk systems. Gray spectra show the observed MOSFIRE data, while dark blue spectra show those data smoothed by a Gaussian filter with a standard deviation of 5. The Gaia J0611–6931 *Flamingos-2* spectra are shown in orange. Metal emissions from Mg I, Fe I, and Si I are detected in Gaia J0611–6931, Gaia J0006+2858, and Gaia J2100+2122. We did not identify metal emissions in the MOSFIRE spectrum of WD 0145+234. The vertical dotted lines mark the centroid of each emission feature, as listed in Table 3. Magenta lines mark Mg I emissions, yellow lines mark Fe I emissions, blue mark Si I emissions, and dark green mark unknown emissions.

I, and possibly Fe I. These emission lines are highlighted for each system in Figure 3. The FWZI values are mostly consistent within each system, with the exception of a few

lines that are likely a blend of several transitions. For example, the Mg I line at $1.5029 \mu\text{m}$ had a much larger FWZI than any of the other lines observed in Gaia J0006+2858. We attribute this

Table 3
Observed Emission Lines

Transition (Vacuum μm)	E_{high} (eV)	$\log(gf)$	Gaia J0006+2858			Gaia J0611–6931			Gaia J2100+2122		
			EW (\AA)	FWZI (km s^{-1})	RV (km s^{-1})	EW (\AA)	FWZI (km s^{-1})	RV (km s^{-1})	EW (\AA)	FWZI (km s^{-1})	RV (km s^{-1})
Magnesium											
Mg I 1.1831	5.3937	−0.3319	4.2 ± 0.8	1551 ± 220	-10 ± 46	10 ± 2	3226 ± 560	228 ± 109	1.2 ± 0.5	1686 ± 503	20 ± 101
Mg I 1.2086	6.7790	0.3733	8.6 ± 1.9	2536 ± 464	248 ± 109	0.3 ± 0.1	724 ± 115	22 ± 25
Mg I 1.4882 ^a	6.7790	0.6978	4.9 ± 2.1	1452 ± 494	b	15 ± 2	3558 ± 447	b
Mg I 1.5029	5.9328	0.3577	25 ± 2	1973 ± 125	b	40 ± 3	2400 ± 122	b
Mg I 1.5044	5.9320	0.1355	b	b	b	b	b	b
Mg I 1.5052	5.9320	−0.3422	b	b	b	b	b	b
Mg I 1.5745	6.7190	−0.2118	6.9 ± 1.3	1198 ± 179	b	12 ± 1	1918 ± 139	b	2.1 ± 0.6	1019 ± 233	b
Mg I 1.5753	6.7190	0.1402	b	b	b	b	b	b	b	b	b
Mg I 1.5770	6.7190	0.4108	b	b	b	b	b	b	b	b	b
Mg I 1.7113	6.1182	0.0648	2.4 ± 1.1	1491 ± 549	-201 ± 107	5.8 ± 1.4	1928 ± 363	-35 ± 86
Silicon											
Si I 1.1987	5.9639	0.1775	4.6 ± 0.8	1395 ± 257	b	26 ± 3	3592 ± 277	b	1.5 ± 0.4	1702 ± 390	b
Si I 1.1994	5.9537	−0.1720	b	b	b	b	b	b	b	b	b
Si I 1.2034	5.9840	0.4181	3.2 ± 0.8	1456 ± 291	b	b	b	b
Si I 1.2107	5.9537	−0.3948	b	b	b	b	b	b
Si I 1.2274	5.9639	−0.4379	1.8 ± 0.7	1818 ± 520	-1.4 ± 103	4.9 ± 0.8	2165 ± 266	73 ± 51
Si I 1.5893	5.8624	−0.0068	6.6 ± 1.8	1561 ± 327	-26 ± 66	24 ± 2	4011 ± 236	94 ± 47	5.8 ± 1.1	2501 ± 384	25 ± 77
Si I 1.5964	6.7606	0.1976	3.1 ± 1.6	1309 ± 524	-131 ± 100	b	b	b	3.2 ± 0.7	1204 ± 187	65 ± 39
Si I 1.6385	6.6192	−0.2718	9.2 ± 1.2	3697 ± 396	165 ± 75
Si I 1.6386	6.7206	−0.4225	b	b	b
Iron^b											
Fe I 1.1886	3.2410	−1.6676	2.6 ± 0.8	1211 ± 223	-100 ± 48	b	b	b	0.7 ± 0.2	933 ± 242	-12 ± 105
Fe I 1.1976	3.2112	−1.4828	b	b	b	b	b	b	b	b	b
Unidentified											
			EW (\AA)	FWZI (km s^{-1})	λ (μm)	EW (\AA)	FWZI (km s^{-1})	λ (μm)	EW (\AA)	FWZI (km s^{-1})	λ (μm)
?			4.4 ± 1.2	1361 ± 320	1.67834 ± 0.0032	5.0 ± 0.9	1737 ± 237	1.67842 ± 0.0027
?			4.2 ± 1.0	825 ± 149	1.68767 ± 0.0012	5.9 ± 0.8	1371 ± 139	1.68750 ± 0.0013

Notes. We did not identify any emission features from GaiaJ0052+4505, WD 0145+234, GaiaJ0723+6301, or GaiaJ0603+4518, and they have been omitted from this table. We could not disentangle some sets of nearby emissions, so we denote each line that is blended with the line listed above it in that wavelength region as “b.” Any RV measurement of a blended line is also listed as “b.”

^a The measurements for this feature are a blend of up to five Mg I emissions with the same E_{high} located between 1.4881 μm and 1.4882 μm . We list the $\log(gf)$ of the highest-probability transition.

^b The Fe I 1.1886 line we identified is blended with the Mg I 1.1831 line in Gaia J0611–6931. The Fe I 1.1976 line we identified is blended with the Si I 1.1987 and 1.1994 lines in all three systems.

to other nearby Mg I lines (1.5044 and 1.5051 μm) that could be blended with the line. Also, the two sets of close Si I lines (1.1987 and 1.2034 μm , 1.5892 and 1.5964 μm) in Gaia J0611–6931 are blended, so we report combined measurements of FWZI and EW for them. The 1.1976 μm Fe I line is blended with the 1.1987 and 1.2034 μm Si I lines in the Gaia J0006+2858, Gaia J0611–6931, and Gaia J2100+2122 spectra, so we treat Fe I as tentative detections in Table 3. There are also two unidentified emission lines that we list in Table 3.

The RV values that we measured among each system varied between different transitions, and they had higher uncertainties than those reported in optical studies of these systems (Dennihy et al. 2020; Melis et al. 2020). We attribute this to the low spectral resolutions in our data compared to optical observations of these systems, as well as the blended nature of many of the lines we observed, causing the centroids of individual lines and velocity shifts to be blurred. For these reasons, we did not compare our measured RV values with those reported in Melis et al. (2020) and Dennihy et al. (2020) as a validity check for our line identifications.

3.2. Brown Dwarf Features

In the spectra of Gaia J0052+4505 and Gaia J0603+4518, we identified broad absorption bands consistent with molecular features from the atmospheres of brown dwarfs. In order to assess these broad spectral features, the flux contribution from the white dwarf had to first be removed. White dwarf model spectra were calculated with parameters listed in Table 1 and calibrated to flux units using optical photometry from PanSTARRS (Chambers et al. 2016) or SkyMapper (Onken et al. 2019). To subtract the white dwarf model from the observed spectroscopy, the model spectrum was interpolated to the observed wavelength grid of each spectrum.

In Figure 4, we identify an H₂O absorption band in the MOSFIRE spectra of Gaia J0052+4505. This feature is observed longward of 1.33 μm , and is present in late-M dwarfs and later dwarf types (McLean et al. 2003). In the *K* band, we clearly detected the CO-band head in the MOSFIRE spectra of both Gaia J0052+4505 and Gaia J0603+4518. This feature is known for its strong absorption longward of 2.3 μm , and is prominent in the spectra of M dwarfs, L dwarfs, and early T dwarfs (McLean et al. 2003). However, we did not observe this feature in the GNIRS spectrum of Gaia J0603+4518. We defer the discussion of this to Section 5.4.

The GNIRS spectrum of Gaia J0723+6301 was mostly consistent with the white dwarf model. In fact, the infrared excess does not start until the *K* band, as shown in Figure 4.

4. Model Fitting

4.1. Dust Disk Model Fitting

The infrared excesses were fit using the dust disk model outlined in Jura (2003). This model describes a flat, opaque ring of blackbody-emitting dust, where the dust’s effective temperature depends only on its orbital radius. Such a dust ring is characterized by three disk parameters: inner radius (R_{in}), outer radius (R_{out}), and inclination angle (i). Given the degeneracies among these three parameters in previous applications (e.g., Jura et al. 2007), we decided to use a Markov Chain Monte Carlo (MCMC) technique to fully explore the parameter space, using the emcee Python module

(Foreman-Mackey et al. 2013). The two parameters describing disk radii (R_{in} and R_{out}) were uniformly sampled in logarithmic space, to avoid potential sampling bias from the nonlinear relationship between the disk radius and temperature. Inclination was uniformly sampled between 0° and 90°. A lower boundary was placed on R_{in} at a sublimation radius where the dust ring temperature is 2500 K, a temperature above which all dust would be expected to sublimate (Steckloff et al. 2021). An upper boundary was placed on R_{out} at a tidal radius of $300R_{\text{WD}}$, a loose constraint for the Roche limit expected for these white dwarfs (Steckloff et al. 2021). The MCMC chains were run using 100 walkers, each with 10,000 steps including a 5000 step burn-in phase.

We fit each system using the new infrared spectroscopic data along with Spitzer 3.6 and 4.5 μm photometry. Given the large difference in wavelength coverage and sampling between the photometry and spectroscopy, in order to combine the two for fits, a weighting factor was added to the likelihood function of the MCMC framework. Each spectroscopy and photometry point was given a weight proportional to its wavelength coverage. We report the median values for each model parameter from these fits with 1σ uncertainties in Table 4. The best-fit models for the dust disks are shown in Figure 5 and the corner plots are in the Appendix.

We also performed the same MCMC fitting routine using the near-infrared (NIR) photometry in Table 5 to compare with the results of our spectroscopic fits. We found that there was very little difference between the photometry-only fits (JHK and Spitzer photometry) and the fits with NIR spectroscopy and Spitzer photometry. We believe this is due to the similar weighting of NIR photometry points and the spectral data, which, when fit with the Spitzer data, resulted in a similar ability to constrain the model parameters. We tested fits with only NIR photometry or spectroscopy, excluding Spitzer points, and found in this scenario that spectroscopy was able to constrain the model parameters better than photometry. Given this, we believe the best combination of data to fit is the NIR spectroscopy with the Spitzer data.

In our analysis of the MCMC dust disk fits, we noted several patterns among the model parameters (i , R_{in} , and R_{out}) across each of the systems we fit. The inner radius was always the best-constrained parameter in our fits of all the systems. This is expected, as the near-infrared is most sensitive to the warmest region of the dust disk near the inner radius. We found that, for all of the disk systems, the temperatures of the inner disk radius were within a reasonable range for dust sublimation, falling between 1200 and 1900 K.

The spread in the posterior distributions of disk inclinations was usually large; the only exception is Gaia J0611–6931, whose large excess flux forced a face-on disk. The spread is due to the inclination’s degenerate nature with the inner and outer radii of the disk. In most of the systems, again with the exception of Gaia J0611–6931, we saw a correlation between i and R_{out} , where larger inclination angles corresponded to larger values of R_{out} . We saw the opposite correlation between i and R_{in} , where larger inclination angles corresponded to smaller values of R_{in} . These correlations are illustrated in the corner plots in the Appendix. Conceptually, the correlation in these parameters is to be expected, as a more face-on disk would require a smaller emitting area to model the same SED as a more edge-on disk with a larger emitting area.

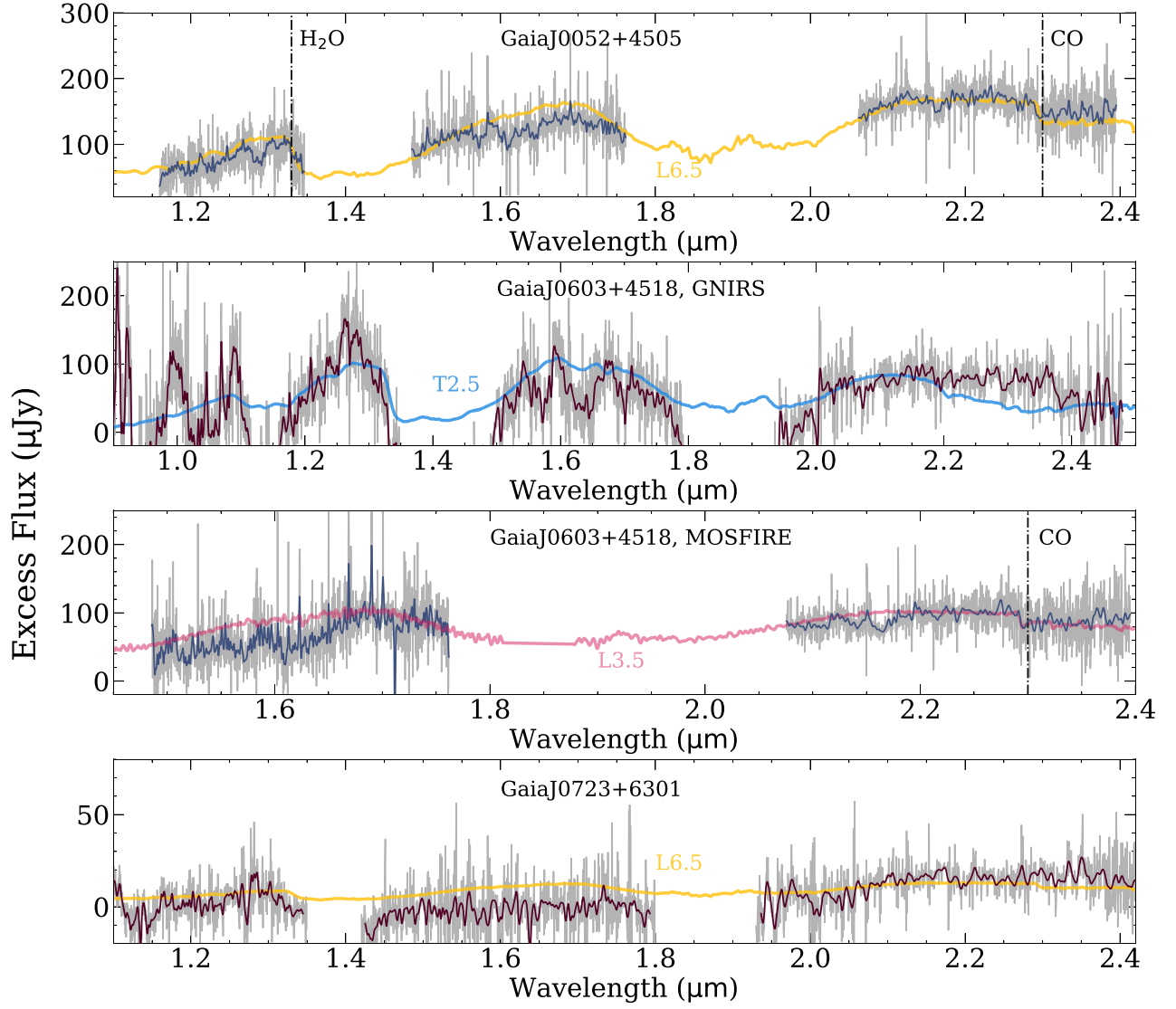


Figure 4. Near-infrared spectra for the two putative brown dwarf companion systems (Gaia J0603+4518, Gaia J0052+4505) and Gaia J0723+6301. The white dwarf contribution has been subtracted, isolating the excess flux. The original spectrum is shown in gray, along with a Gaussian-smoothed version in color. Each spectrum is shown with a best-fitting brown dwarf template spectrum for comparison, as described in Section 4.3. Vertical black dotted lines indicate brown dwarf atmospheric absorption features.

Table 4
Median Dust and Gas Disk Model Parameters and Best-fitting Brown Dwarf Companion

Name	Inclination (deg)	$R_{\text{dust,in}} (R_{\text{WD}})$	$R_{\text{dust,out}} (R_{\text{WD}})$	$v_{\text{in}} \sin i$ (km s $^{-1}$)	$v_{\text{out}} \sin i$ (km s $^{-1}$)	$R_{\text{gas,in}} (R_{\text{WD}})$	$R_{\text{gas,out}} (R_{\text{WD}})$	BD Fit	Likely IR Source
Gaia J0006+2858	66^{+6}_{-33}	20^{+4}_{-4}	64^{+105}_{-24}	545	230	22^{+8}_{-13}	92^{+32}_{-55}	$L6.5 \pm 4.5$	Disk
Gaia J0052+4505	42^{+23}_{-28}	$5.7^{+0.7}_{-0.5}$	$7.4^{+1.2}_{-0.8}$	$L6.5 \pm 4.0$	BD
WD 0145+234	30^{+21}_{-20}	13^{+1}_{-1}	24^{+4}_{-2}	640	358	8^{+8}_{-7}	22^{+23}_{-20}	$L6 \pm 4$	Disk
Gaia J0603+4518									
MOSFIRE	73^{+12}_{-43}	11^{+2}_{-2}	15^{+6}_{-3}	$L3.5 \pm 3.5$	BD
GNIRS	73^{+13}_{-40}	11^{+4}_{-3}	15^{+8}_{-4}	$T2.5 \pm 2.5$	BD
Gaia J0611-6931	$3.6^{+4.0}_{-2.6}$	$10.0^{+0.2}_{-0.2}$	165^{+83}_{-57}	650	313	$0.28^{+0.20}_{-0.27}$	$1.1^{+0.8}_{-1.0}$	$L7 \pm 4$	Disk
Gaia J0723+6301	75^{+10}_{-42}	23^{+8}_{-8}	39^{+74}_{-12}	$L6.5 \pm 4$?
Gaia J2100+2122	60^{+15}_{-35}	33^{+4}_{-6}	57^{+42}_{-9}	370	230	48^{+26}_{-36}	117^{+64}_{-88}	$L6 \pm 4$	Disk

Notes. Dust disk model fits included NIR spectra with Spitzer photometry. Brown dwarf companion fits included NIR spectra only. Errors for the disk model parameters are the 84.1 and 15.9 percentile values (1σ) from each parameter's MCMC posterior distribution. Gas disk calculations are omitted for systems lacking metal emissions. Details for each model are described in Section 4. Gaia J0603+4518 was observed with MOSFIRE and GNIRS, which are reported separately in this table.

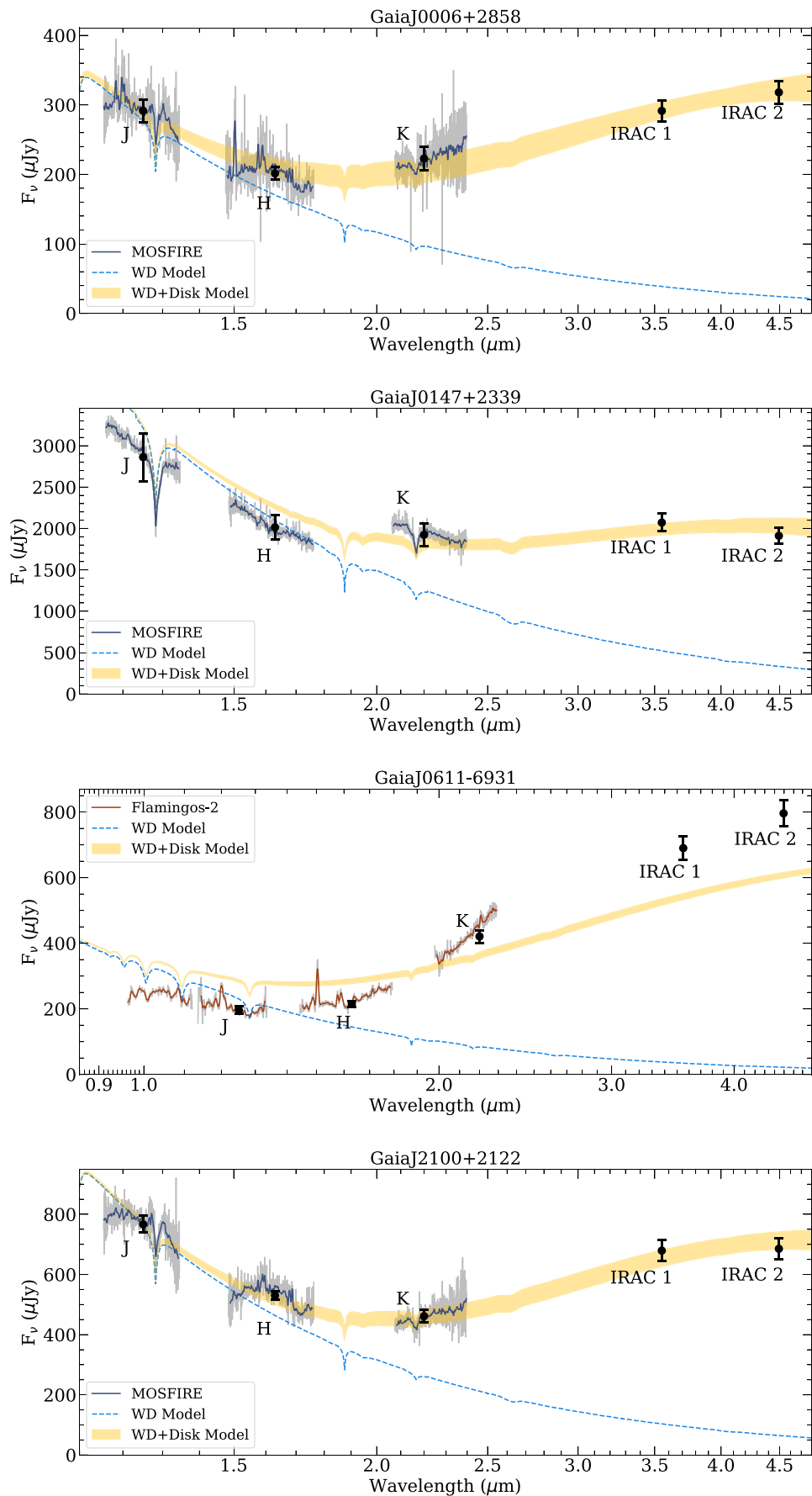


Figure 5. The four dust disk systems, plotted with their median-fit dust model and 1σ uncertainty region, along with a white dwarf model spectrum. The disk parameters are listed in Table 4.

Table 5
Infrared Photometry

Name	J (mag)	H (mag)	K (mag)	IRAC Ch1 (mag)	IRAC Ch2 (mag)
Gaia J0006+2858	16.80 ± 0.06	16.76 ± 0.05	16.13 ± 0.08	14.96 ± 0.06	14.38 ± 0.06
Gaia J0052+4505	16.02 ± 0.05	16.03 ± 0.03	15.61 ± 0.04	15.43 ± 0.06	15.39 ± 0.06
WD 0145+234	14.32 ± 0.11	14.26 ± 0.08	13.79 ± 0.08	12.83 ± 0.06	12.43 ± 0.06
Gaia J0603+4518	15.40 ± 0.04	15.43 ± 0.02	15.33 ± 0.03	14.97 ± 0.06	14.92 ± 0.06
Gaia J0611–6931	17.23 ± 0.06	16.69 ± 0.05	15.44 ± 0.05	14.13 ± 0.06^a	13.34 ± 0.06^a
Gaia J0723+6301	17.36 ± 0.43	17.37 ± 0.35	17.04 ± 0.15	16.39 ± 0.06	16.05 ± 0.06
Gaia J2100+2122	15.75 ± 0.04	15.71 ± 0.03	15.34 ± 0.05	14.04 ± 0.06	13.54 ± 0.06

Notes. Photometry is from Lai et al. (2021), except for Gaia J0611–6931, which is from Denny et al. (2020). The JHK magnitudes are reported in the MKO system.

^a These are WISE magnitudes, because the Spitzer data were marked as potentially spurious in Denny et al. (2020).

The posterior distributions for the outer radius parameter consistently showed a peak at a smaller value, with an unconstrained tail going to larger radii. This was expected due to the lack of longer-wavelength data. The outer radius is the coolest part of the disk, to which the mid-infrared is much more sensitive than the near-infrared. If there were available spectral data for these systems at wavelengths longer than our Spitzer photometry, our ability to constrain this parameter would greatly improve.

When we compared the posterior distributions for each disk parameter between the disk systems and the likely brown dwarf companion systems, we found some differences with the best-fitting disk radii that can be seen in the corner plots in the Appendix. The R_{in} distribution for each of the likely brown dwarf companion systems was close to the dust sublimation limit. This can be seen in the corner plots with the sharp cutoff on the lower end of each R_{in} distribution. Hot disks were required to fit the beginning of excess flux at shorter wavelengths, a trait of brown dwarf companion systems (Lai et al. 2021). We also found that these systems were fit by narrower disks, with the R_{out} distributions close to the best-fitting R_{in} .

4.2. Gas Disk Model Fitting

Using metal emission lines observed in four of our systems (Gaia J0006+2858, WD 0145+234, Gaia J0611–6931, and Gaia J2100+2122), we calculated the inner and outer radius of the emitting gas region for each system. In order to make this calculation, we assumed that the gas in each system is orbiting the white dwarf in a circular disk and has the same inclination in our line of sight as the dust. Disk formation models suggest that such assumptions are reasonable, as gaseous material can be formed either from impacts between bodies within the dust disk or from dust sublimation at the hot inner edge of the disk, spreading throughout the disk from there (Jura 2008; Melis et al. 2010; Rafikov 2011a; Bochkarev & Rafikov 2011; Hartmann et al. 2011; Rafikov 2011b; Metzger et al. 2012; Bear & Soker 2013; Hartmann et al. 2016; Kenyon & Bromley 2017a).

With our assumptions about the geometry of the emitting gas disks in our systems, we related observed properties of the emissions to the inner and outer radius of each gas disk. The fastest-moving gas located at the disk’s inner radius is related to half of the full width of a gas emission line, which we list as $v_{\text{in}} \sin i$ in Table 4. On the other hand, when double-peaked line profiles are observable, peak separation is about twice the velocity at the outer radius of emitting gas ($v_{\text{out}} \sin i$).

While Melis et al. (2020) measured these properties for the four gas-emitting systems in this paper, they warned against drawing such conclusions about the disk geometry without sufficiently modeling the dust portion and viewing angle of the debris disk. Our MCMC fitting technique of the infrared spectra described in Section 4.1 does just this. The resulting posterior distributions for disk inclinations provide us with a reasonable uncertainty range of inclinations based on the observed infrared excess.

While we measured the full widths of the gas emissions we observed in our infrared spectra, which are listed in Table 3, we decided to use the reported values in Melis et al. (2020) for our gas disk calculation because the optical emission lines are well resolved. We listed these values in Table 4.

We found that, for three of our four gas emissions systems (Gaia J0006+2858, WD 0145+234, and Gaia J2100+2122), the gas inner and outer radii were all consistent with our modeled dust disk properties reported in Table 4. The gaseous material appears to spatially coincide with the dust disk, as has been found in other gaseous systems (Melis et al. 2010).

The calculated gas inner and outer radii of one system, Gaia J0611–6931, stand out as being unreasonably small and in disagreement with the best-fitting dust disk properties for the system. This can be attributed to our dust disk model’s inability to sufficiently reproduce the strong brightness of infrared excess observed in this system. Our model was forced to a face-on disk for this system, meaning the inclination range we used for our gas disk calculation resulted in unreasonable small inner and outer radii. As we expand upon in Section 5.5, the measured properties of this system require a more complex disk model than the flat disk model that we use in this paper.

4.3. Brown Dwarf Template Comparison

We also compare the excess spectra from all of our systems with template spectra of field brown dwarfs. These templates were collected from the IRTF (Cushing et al. 2005) and SpeX libraries (Cruz et al. 2004; Chiu et al. 2006; Kirkpatrick et al. 2006; Siegler et al. 2007; Burgasser et al. 2008;Looper et al. 2008; Sheppard & Cushing 2009), which include a total of 325 observed spectra of L and T dwarfs.

To find the best-match brown dwarf companion spectrum for each of the observed spectra, a χ^2 type goodness-of-fit test was used. The observed spectrum was first smoothed with a Gaussian filter as shown in Figure 1 to reduce noise and focus the fit on broad spectral features and the overall shape of the spectrum. For each template brown dwarf spectrum, a goodness-of-fit statistic G was computed as described by Equation

(1) of Cushing et al. (2008). This statistic G was minimized with respect to a scaling factor C multiplied to the flux of each template, to match it to the flux level of the observed spectrum.

To estimate the most likely range of companion spectral types for each system, we ran our comparison algorithm on all the L and T dwarfs in the IRTF and SpeX libraries. For each spectral type, we calculated the mean G value among the template spectra. We then found the lower 32nd percentile (1σ) of average G values among the spectral types, which we report as the likely range of companion spectral types for a given system in Table 4. Since Gaia J0603+4518 had both MOSFIRE and GNIRS data, we report two separate ranges of companions that fit the data from each instrument. The MOSFIRE spectra of Gaia J0052+4505 and Gaia J0603+4518 can be best fit with an L dwarf. The GNIRS spectrum of Gaia J0603+4518 can be best fit with a T dwarf. We discuss this discrepancy between the Gaia J0603+4518 MOSFIRE and GNIRS data in Section 5.4. Even though the Gaia J0723+6301 spectrum can be best fit by an L dwarf, the lower 1σ G value is significantly higher compared to the other two systems, pointing to the fact that this system’s spectrum was not fit well by any of the potential companions.

Interestingly, the excess flux of all the disk systems can also be fit with an L-dwarf template. However, their goodness-of-fit G values are much bigger than the likely brown dwarf systems (see the Appendix for details).

So far, the majority of unresolved white dwarf–brown dwarf pairs have been identified via systematic searches of white dwarfs for an infrared excess (e.g., Debes et al. 2011; Girven et al. 2011; Steele et al. 2011). These systems were then confirmed via radial velocity measurements (e.g., Maxted et al. 2006; Steele et al. 2013). The radial velocity measurements can only detect systems with a short period, and hence high radial velocity. It is also often difficult to obtain high-precision radial velocity measurements because it is hard to determine the centroid of broad Balmer lines in white dwarfs’ atmospheres. One must also only use short exposures to avoid smearing the fast-moving lines, which is often challenging for these faint systems. In the most irradiated binaries, there is emission seen from the brown dwarf atmosphere, allowing measurements from both components (e.g., WD0137-349AB; Casewell et al. 2015). Since the launch of Kepler and now with ZTF, there have been more systems discovered to be eclipsing. These short-period systems have deep, total eclipses where the Jupiter-sized brown dwarf completely obscures the Earth-sized white dwarf (e.g., Parsons et al. 2017; Casewell et al. 2020; van Roestel et al. 2021). However, both of these methods of discovering binaries can be time consuming. It is not feasible to obtain a ~ 10 hr lightcurve (or longer) of every white dwarf, nor multiple epochs of spectroscopy in the hope of finding a companion.

Characterizing the infrared excess around white dwarfs is a much more efficient method to detect new white dwarf–brown dwarf pairs (e.g., Rebassa-Mansergas et al. 2022).

5. Discussion

5.1. Gaia J0006+2858

Optical observations of Gaia J0006+2858 have shown a rich set of emission features from Ca II, Fe II, O I, and possibly Mg I. These emission lines are unique in the significant asymmetry of their maximum blue and red velocities (Melis et al. 2020). In the infrared spectra, we identified emission lines from Mg I, Si

I, and possibly Fe I, all of which are new detections. We also observed unidentified emissions near 1.6784 μm and 1.6875 μm , which were also seen in Gaia J2100+2122 (Table 3). The FWZIs of the infrared lines listed in Table 3 are around 1400 km s^{-1} , which are generally consistent with those in the optical. The strongest infrared emission line is Mg I 1.5029 μm , which has an EW of 24 \AA . This is even stronger than the Ca II 8542 \AA emission from Melis et al. (2020), which had an EW of 19.2 \AA , and is typically the strongest emission feature in white dwarf gas disks. However, the Mg I 1.5029 μm line may be blended with nearby Mg I 1.5044 and 1.5051 μm lines, which contribute to the large FWZI of 1973 km s^{-1} .

In addition to the new metal species identified in this system, our MCMC disk fit was able to model this system’s infrared excess well, with excess beginning in the H band as shown in Figure 5. The median-fit disk model for this system extends from 20 R_{WD} to 64 R_{WD} , with an inclination 66° . Our fit was able to constrain the inner edge of the disk particularly well, with the upper and lower 1σ region of the posterior distribution being only 4 R_{WD} .

Gaia J0006+2858 also has a heavily polluted atmosphere, including detection of Ca, Mg, and Si (Rogers 2023). The atmospheric pollution and strong metal emission lines show that this white dwarf hosts a dust disk.

5.2. Gaia J0052+4505

We identified broad molecular absorption features in the near-infrared spectrum of this system, indicative of a brown dwarf companion. In the J band, we identified H_2O absorption longward of 1.33 μm . In the K band, we observed the CO-band head beginning at 2.3 μm . Both of these features are prominent in the spectra of brown dwarf atmospheres. We show these in Figure 4, along with field brown dwarf spectra as a comparison.

We found that a brown dwarf companion was the most likely source of infrared excess flux for this system, given all of our observed data. Our goodness-of-fit tests on the morphology of this system’s spectrum found that the most likely companion is an $\text{L}6.5 \pm 4.0$ type brown dwarf. We note that the H -band photometry for this system does not match up with the best-fitting brown dwarf model in Figure 6. In Section 5.4, we demonstrate that spectral variability may be seen for the other white dwarf–brown dwarf system, Gaia J0603+4518. Because our photometric observations could have been taken at different phases of the companion’s orbit, it is possible that we are seeing variability in the photometry here, if this is a tight, possibly tidally locked, system (Lew et al. 2021).

Our analysis of the Keck/HIRES optical spectrum also did not find evidence of atmospheric pollution on the white dwarf. This lack of accretion further supports a brown dwarf companion being the source of infrared excess in this system.

5.3. WD 0145+234

The infrared spectrum of WD 0145+234 only shows absorption lines from the white dwarf’s atmosphere. We did not identify any emission or absorption features. This is not particularly surprising, as previous optical studies only reported weak Ca II emissions (Melis et al. 2020). Most interestingly, this system was discovered to be going through an ongoing burst in the mid-infrared by Wang et al. (2019). The system had brightened by about 1.0 mag in the $W1$ and $W2$ bands within half a year, while remaining the same in optical photometry. This led to the

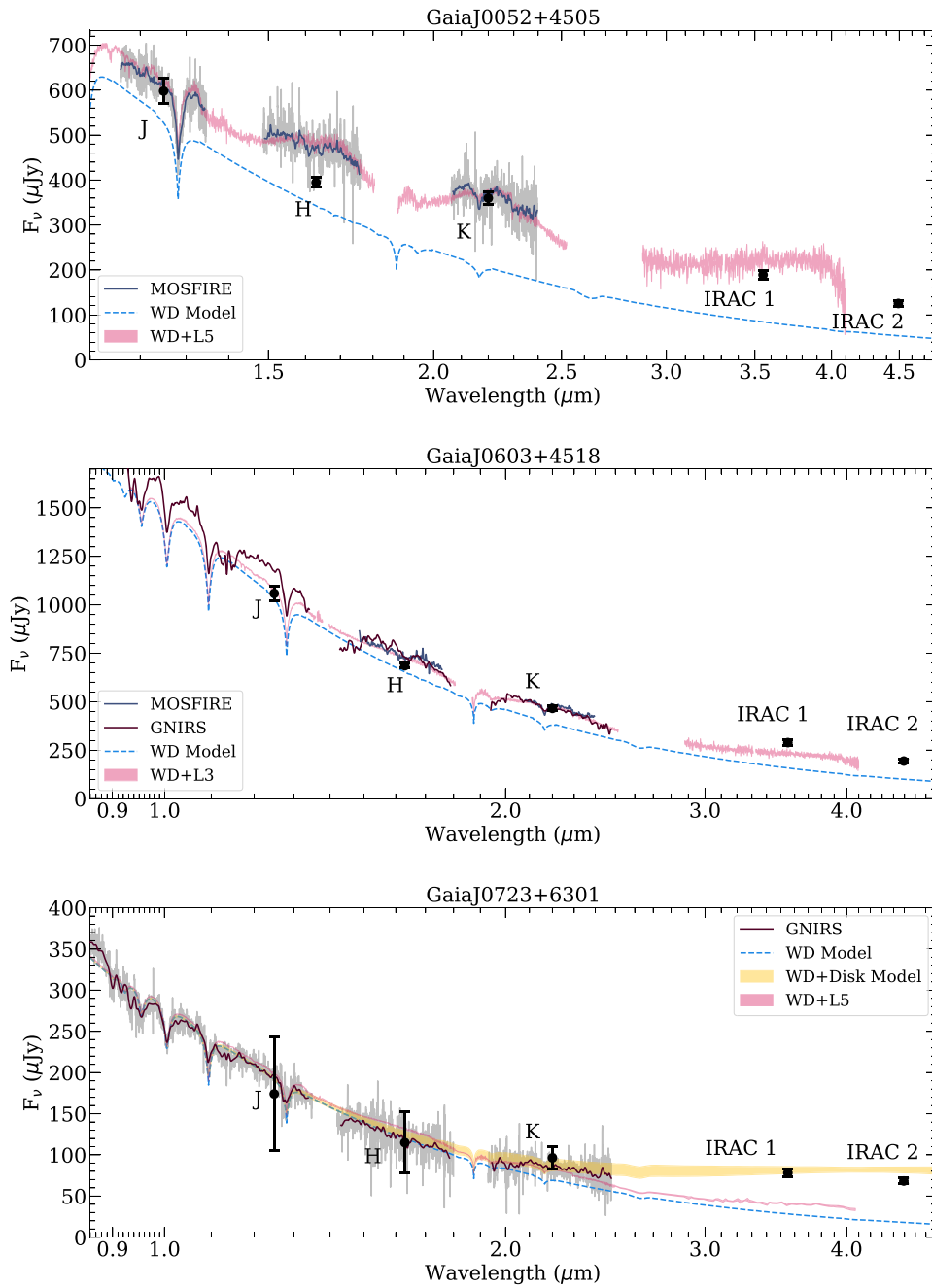


Figure 6. The two brown dwarf companion systems (Gaia J0052+4505 and Gaia J0603+4518) and Gaia J0723+6301, plotted with their best-fit brown dwarf companion template spectrum. We also show the best-fit disk model for Gaia J0723+6301.

conclusion that the outburst was most likely due to a planetesimal being tidally disrupted, adding new material to an existing quiescent disk. WD 0145+234 is also heavily polluted, with a high calcium accretion rate (as shown in Table 3).

As shown in Figure 5, our best-fit disk model cannot reproduce all the observed photometry points. The larger variability in the WISE bands suggests strong variability in the Spitzer and *JHK* bands as well, which complicates the analysis for this system because the *JHK* photometry and Spitzer photometry were taken at different times.

We conclude that the infrared excess around WD 0145+234 comes from a dust disk due to the presence of strong infrared variability, a featureless infrared spectrum, and a heavily polluted atmosphere.

5.4. Gaia J0603+4518

As with Gaia J0052+4505, we identified broad molecular absorption features in the near-infrared spectrum of this system, indicating the presence of a brown dwarf companion. We observed H₂O absorption beginning at 1.33 μm in our GNIRS spectrum, as well as the CO-band head beginning at 2.3 μm in the *K* band of our MOSFIRE spectrum. We show these in Figure 4, along with field brown dwarf spectra as a comparison.

We could not make a clear detection of the CO-band head in the GNIRS spectrum of this object. The spectral resolution of GNIRS is lower than that of MOSFIRE, making it harder to detect weak features. Alternatively, this may be due to variability from viewing the dayside and nightside of a tidally locked brown dwarf companion. Near-infrared studies of other

irradiated brown dwarfs in white dwarf binaries have shown a high level of wavelength-dependent variability in the flux contribution from the brown dwarfs, especially with respect to regions of molecular absorption. For example, Lew et al. (2021) found the $1.3 \mu\text{m}$ H₂O band to vary 10 times more than the rest of the *J* band, in a brown dwarf irradiated by a white dwarf. In another similar system, Casewell et al. (2018) observed a significant amount of variability between dayside and nightside *K*-band photometry, where the CO-band head is located. The effective temperature of this white dwarf is comparable to WD 0137-349, which hosts an irradiated brown dwarf with observed variability in optical and near-infrared photometric studies (Casewell et al. 2015; Zhou et al. 2022). This further demonstrates the plausibility of Gaia J0603+4518 hosting a similarly irradiated brown dwarf companion. Future observations with time-series infrared spectroscopy would give a better understanding of how the CO-band head is affected by irradiation in a tight white dwarf–brown dwarf binary system.

In addition, we observed some differences in the overall morphology between the MOSFIRE and GNIRS spectra. In our comparison tests with template brown dwarf spectra, as described in Section 4.3, these morphological differences resulted in slightly different best-fitting companions for the two spectra. Our tests found that the MOSFIRE spectrum best followed an early to late L dwarf, while the GNIRS spectrum best followed a late L to early T dwarf.

Our modeling of the MOSFIRE and GNIRS spectra of this system found a brown dwarf companion to be more likely than a debris disk as the source of infrared excess, which begins in the *J* band. The goodness-of-fit test for the MOSFIRE data estimates this companion to be an $L3.5 \pm 3.5$ type brown dwarf, while the GNIRS spectrum favored a $T2.5 \pm 2.5$ (see the Appendix for details). We again believe that these differences in the morphology of the spectrum between the two instruments for this system are due to observing the brown dwarf companion in different phases of its orbit, as the two epochs of data were taken about a year apart.

Our analysis of the Keck/HIRES optical spectrum did not find evidence of atmospheric pollution on the white dwarf. This lack of accretion further supports the scenario of a brown dwarf companion being the source of infrared excess in this system. Gaia J0603+4518 appears as one single object in the GNIRS and MOSFIRE data, which means the companion must be within $0''.7$ (projected separation of 42 au) of the white dwarf.

5.5. Gaia J0611–6931

We identified strong emission lines from Mg I, Si I, and possibly Fe I in the Flamingos-2 spectrum of Gaia J0611–6931. Previously, emissions features from O I, Na I, Mg I, Si I, Ca II, and Fe II have been reported in the optical spectra (Dennihy et al. 2020; Melis et al. 2020). These infrared Mg I, Fe I, and Si I lines are much stronger than those in the optical. The FWZIs reported in Table 3 are also larger than FWZIs of 1400 km s^{-1} reported in the optical, likely due to blending of several lines. With six different species, Gaia J0611–6931 has the most variety of metal emissions.

In addition to this rich emission spectrum, Gaia J0611–6931 has one of the brightest known infrared excesses from a white dwarf, with a fractional luminosity of 5.16% (Dennihy et al. 2020). While our best-fitting disk model performed better than the best brown dwarf companion, the level of excess from this system could not be reproduced by our model. As shown in

Figure 5, even a wide face-on disk fails to produce the strong infrared excess. Relaxing the physical constraints on the disk’s inner and outer disk radius did not improve the fit. Dennihy et al. (2020) suggested that the strength of this excess would require a model with multiple dusty components rather than a flat dust disk model. Simulations show that the disk could retain a large scale height under collisional cascade (Kenyon & Bromley 2017b; Ballering et al. 2022).

High-resolution optical spectroscopy has revealed the presence of Ca, O, Mg, Si, and Fe in the white dwarf atmosphere (Rogers 2023). The presence of a strong infrared excess, the detection of multiple metal emission features, and a heavily polluted atmosphere provide convincing evidence that Gaia J0611–6931 hosts a dust disk.

5.6. Gaia J0723+6301

We found the near-infrared spectrum of this system to be consistent with a white dwarf until the *K* band, where excess flux begins (see Figure 6). We did not identify any emission features or broad absorption features indicating either a debris disk or brown dwarf companion.

Our analysis of the Keck/HIRES spectrum of places an upper limit of the calcium mass accretion rate of $7.5 \times 10^5 \text{ g s}^{-1}$. Assuming the calcium mass fraction is 1.62%, taken from bulk Earth (Allègre et al. 2001), in the accreting material, the upper limit to the total mass accretion rate is $4.6 \times 10^7 \text{ g s}^{-1}$, which is very low compared to other dusty white dwarfs (Xu et al. 2019). If the infrared excess comes from a dust disk, Gaia J0723+6301 would have the lowest mass accretion rate among all the dusty white dwarfs.

We also checked the Spitzer/IRAC images of Gaia J0723+6301 for a potential background galaxy causing the infrared excess. The white dwarf is well detected in both IRAC-1 and IRAC-2, and it appears to be isolated. Aperture photometry and Point Response Function photometry return the same flux level for this system (Lai et al. 2021). The GNIRS acquisition image also shows that there are no objects beyond $1''.0$ (projected separation 137.9 au) of the white dwarf. However, we cannot completely rule out the possibility that there is a background galaxy along the line of sight and it only emits in the IRAC bands. In that scenario, the infrared excess around Gaia J0723+6301 is spurious.

From the literature, there is one system in a situation similar to that of Gaia J0723+6301, namely WD 2328+107, which has a subtle infrared excess (Rocchetto et al. 2015) but no atmospheric pollution from Hubble observations (Wilson et al. 2019). There are no infrared spectroscopic observations of WD 2328+107, which would be very useful in characterizing the origin of the infrared excess.

5.7. Gaia J2100+2122

The optical spectrum of Gaia J2100+2122 is dominated by Fe II emission lines, as well as Ca II and O I (Dennihy et al. 2020; Melis et al. 2020). An interesting characteristic of the system is that the emission line strength varied dramatically over the course of a few months, likely due to ongoing gas production or excitation. We have tentative identifications of Mg I, Fe I, and Si I in the MOSFIRE spectrum of this system. As listed in Table 3, the Si I lines are much stronger compared to Mg I and Fe I lines, which is the opposite of Gaia J0611–6931 and Gaia J0006+2858. This may be

explained by different silicon-to-magnesium ratios in the gas debris. We also observed unidentified emissions near 1.6784 and 1.6875 μm , also seen in Gaia J0006+2858.

Given the observed data, we found the most likely scenario for the source of infrared excess in this system to be a dusty debris disk. Fitting the infrared excess flux as a flat disk, we constrained the disk's inner radius to be near $33 R_{\text{WD}}$, with an outer radius likely extending to $57 R_{\text{WD}}$. We show this disk model in Figure 5.

The atmosphere of Gaia J2100+2122 is polluted with Ca, Mg, Fe, and Si (Rogers 2023). The detection of variable metal emissions, a nearly featureless infrared spectrum, and a heavily polluted atmosphere suggest that Gaia J2100+2122 hosts a dust disk.

6. Conclusion

We present near-infrared spectroscopy of seven infrared-excess white dwarf systems. With these new data, we are able to determine the source of infrared excess in six of the white dwarf systems. For the first time, we identified infrared emission features (Mg I, Si I, and possibly Fe I) from the gaseous component of a debris disk around a white dwarf. We also clearly observed broad molecular absorption features from the atmospheres of two unresolved white dwarf–brown dwarf pairs.

We showed, with a high level of confidence, that the sources of infrared excess in four of the white dwarf systems—Gaia J0006+2858, WD 0145+234, Gaia J0611–6931, and Gaia J2100+2122—are dusty debris disks. We detected emissions from Mg I, Si I, and possibly Fe I in the spectra of Gaia J0611+6931, Gaia J0006+2858, and Gaia J2100+2122, which originate from a gaseous component of their debris disks. We also found the best-fitting parameters for a flat dust disk model for each of these systems, which fit the observed data for Gaia J0006+2858 and Gaia J2100+2122 particularly well. Using the best-fitting inclination range from these modeled disks along with optical gas emissions reported in Melis et al. (2020), we were able to calculate the inner and outer radii of emitting gas in the four disk systems. We found that the inner and outer radii of the gas disks were consistent with the best-fitting location of the dust disks for Gaia J0006+2858, WD 0145+234, and Gaia J2100+2122. The infrared excess observed around Gaia J0611–6931 is so strong that the disk cannot be flat. This system will require more complex models of gas and dust debris components in order to reproduce its measured properties.

We found strong evidence for the presence of unresolved brown dwarf companions as the source of infrared excess in two of our systems—Gaia J0052+4505 and Gaia J0603+4518. These systems both showed broad absorption features attributed to molecules in the atmospheres of brown dwarfs. When we compared the observed spectra for each of these systems to a large sample of brown dwarf spectra, we determined the best-fitting companions for Gaia J0052+4505 and Gaia J0603+4518 were L dwarfs.

The source of infrared excess in Gaia J0723+6301 remains a mystery. There is a lack of detectable metal pollution from the Keck/HIRES data, and there are no signs of molecular absorption features that would support the presence of a brown dwarf companion. Thus, we do not have enough evidence to discern the most likely source of excess in this system.

These seven systems come from the larger sample of infrared excess white dwarfs reported in Lai et al. (2021). Future follow-up spectroscopy in the infrared of these systems would

lead to a much better understanding of their occurrence rates, the unique nature of individual systems, and their properties as a population. Observations in even longer wavelengths, such as with the James Webb Space Telescope, will much better constrain the parameters of these systems.

This research made use of `PyPeIt`,¹¹ a Python package for semi-automated reduction of astronomical slit-based spectroscopy (Prochaska et al. 2020, 2020).

We would like to thank Samuel Lai for his help with our questions about the photometry in Lai et al. (2021). D.O. would also like to thank the Gemini-North staff for creating such a welcoming environment to work in during the science internship.

This work is based on observations obtained at the international Gemini Observatory, a program of NSF's NOIRLab, which is managed by the Association of Universities for Research in Astronomy (AURA) under a cooperative agreement with the National Science Foundation on behalf of the Gemini Observatory partnership: the National Science Foundation (United States), National Research Council (Canada), Agencia Nacional de Investigación y Desarrollo (Chile), Ministerio de Ciencia, Tecnología e Innovación (Argentina), Ministério da Ciência, Tecnologia, Inovações e Comunicações (Brazil), and Korea Astronomy and Space Science Institute (Republic of Korea). The data is processed using the Gemini IRAF package. This work was enabled by observations made from the Gemini-North telescope, located within the Maunakea Science Reserve and adjacent to the summit of Maunakea. We are grateful for the privilege of observing the Universe from a place that is unique in both its astronomical quality and its cultural significance.

The data presented herein were obtained at the W. M. Keck Observatory, which is operated as a scientific partnership among the California Institute of Technology, the University of California, and the National Aeronautics and Space Administration. The Observatory was made possible by the generous financial support of the W. M. Keck Foundation. This work is partly supported by the Heising–Simons foundation.

This research has benefited from the SpeX Prism Spectral Libraries, maintained by Adam Burgasser at <http://www.browndwarfs.org/spexprism>.

Facilities: Gemini: Gillett (GNIRS, Flamingos-2), Keck: I (MOSFIRE, HIRES).

Software: Astropy (Astropy Collaboration et al. 2022), emcee (Foreman-Mackey et al. 2013).

Data Availability

The reduced MOSFIRE, GNIRS, Flamingos-2 infrared spectra described in Section 2 and shown in Figure 1 are available in a machine-readable format accompanying this paper. We report the wavelength axis in μm , and the flux axis in Jy.

Appendix

The corner plots for the MCMC modeling described in Section 4.1 are shown in Figures A1 and A2. The goodness-of-fit statistic G described in Section 4.3 is shown in Figures A3 and A4.

¹¹ <https://pypeit.readthedocs.io/en/latest/>

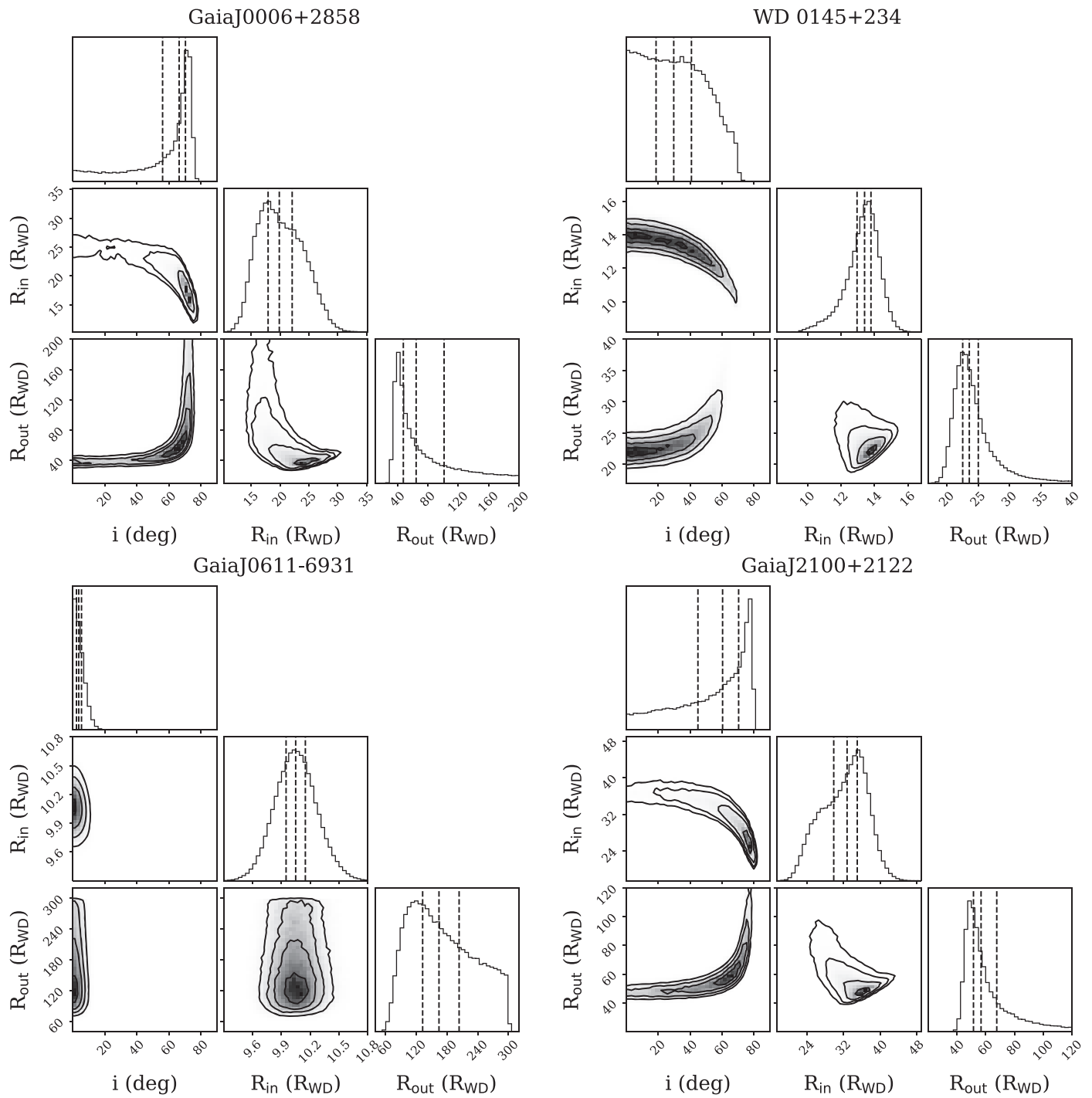


Figure A1. Corner plots from the MCMC fits of the disk systems. The dashed lines mark the median values and 1σ uncertainties. For each system, the inner radius (R_{in}) is generally well constrained.

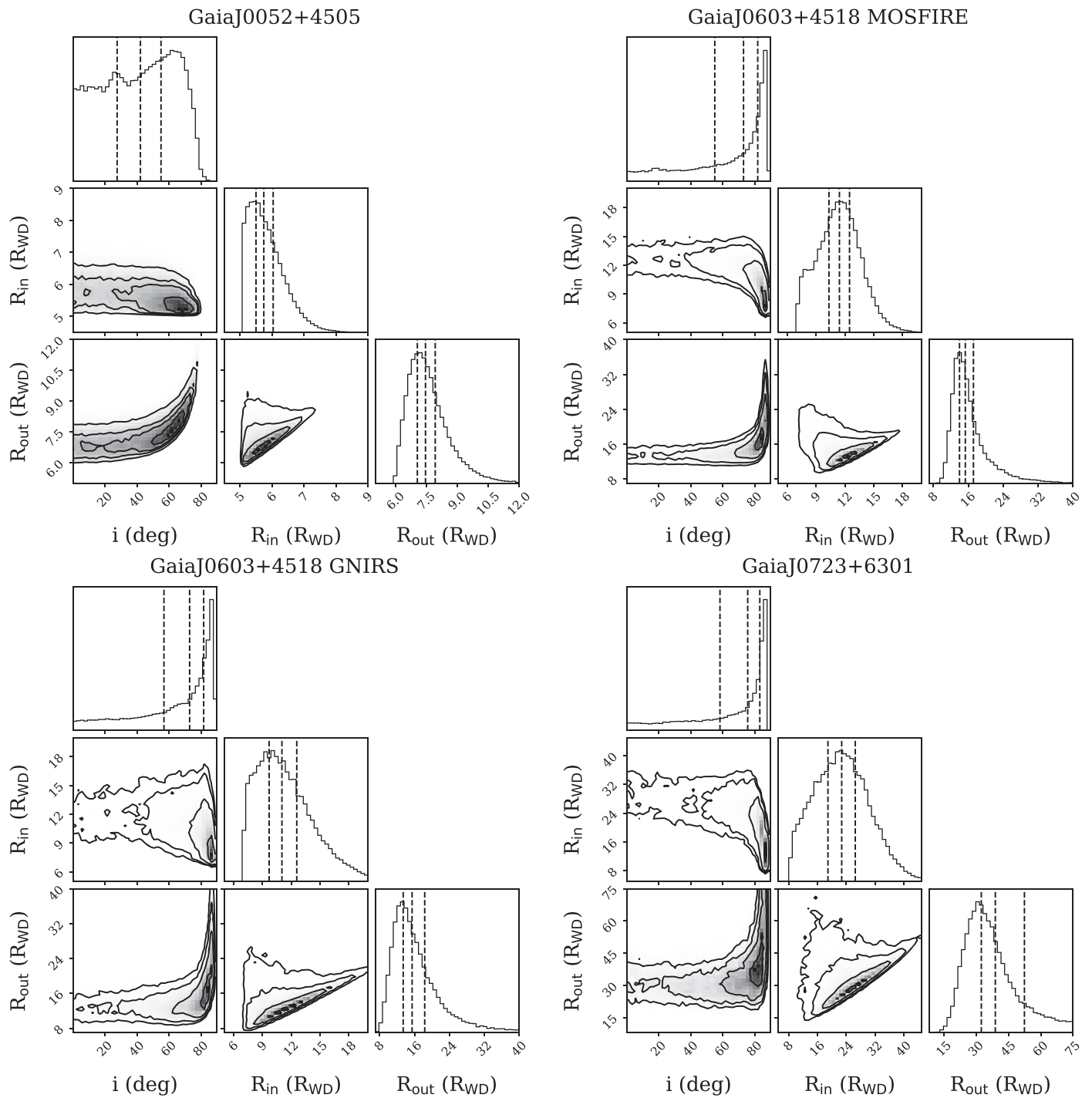


Figure A2. Similar to Figure A1 for the three remaining systems. Compared to the disk systems shown in Figure A1, these infrared excesses can be fit by narrower disks, due to the smaller emitting areas.

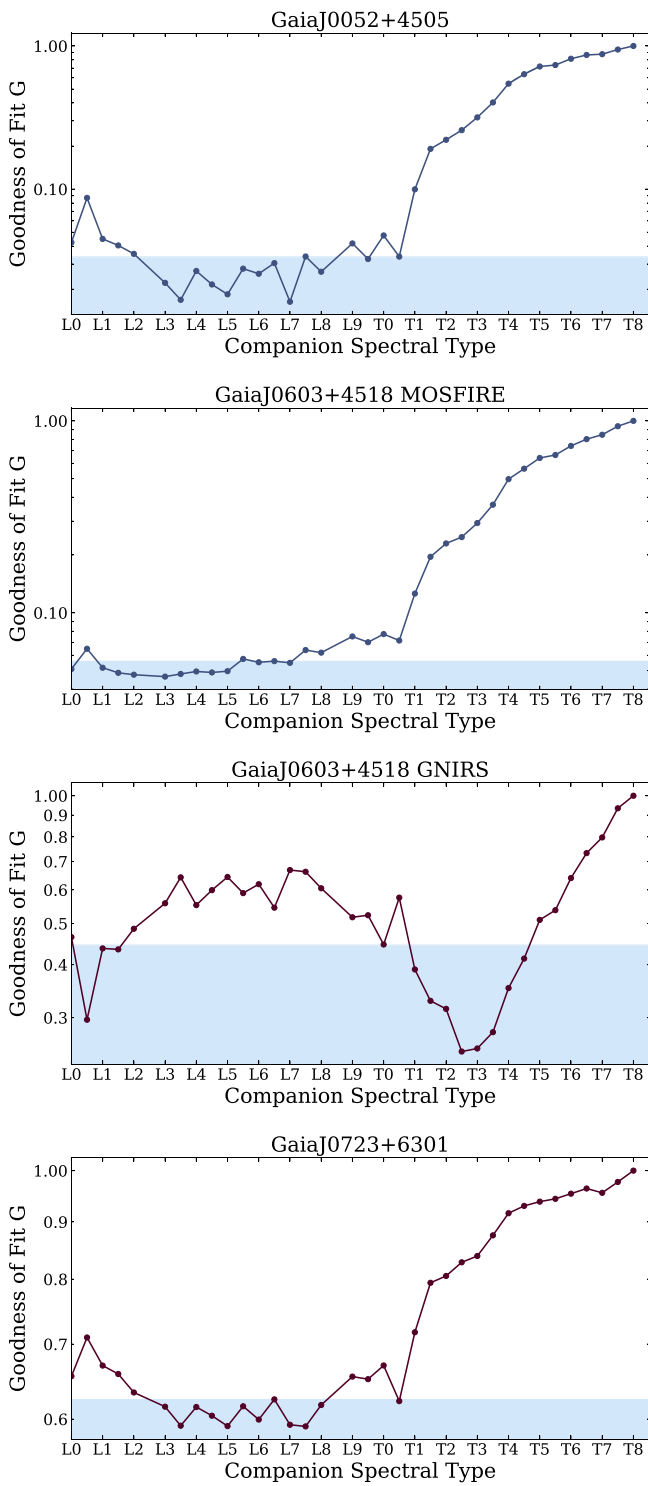


Figure A3. Brown dwarf companion goodness-of-fit statistic, G , plotted against spectral types in the *SpeX* library for the likely brown dwarf companion systems. The blue-shaded region shows the lower 32nd percentile (1σ) of average G values for the spectral types. It is worth noting the different y-axis range for each system, as the Gaia J0723+6301 fits were poor compared to those for Gaia J0052+4505 and Gaia J0603+4518.

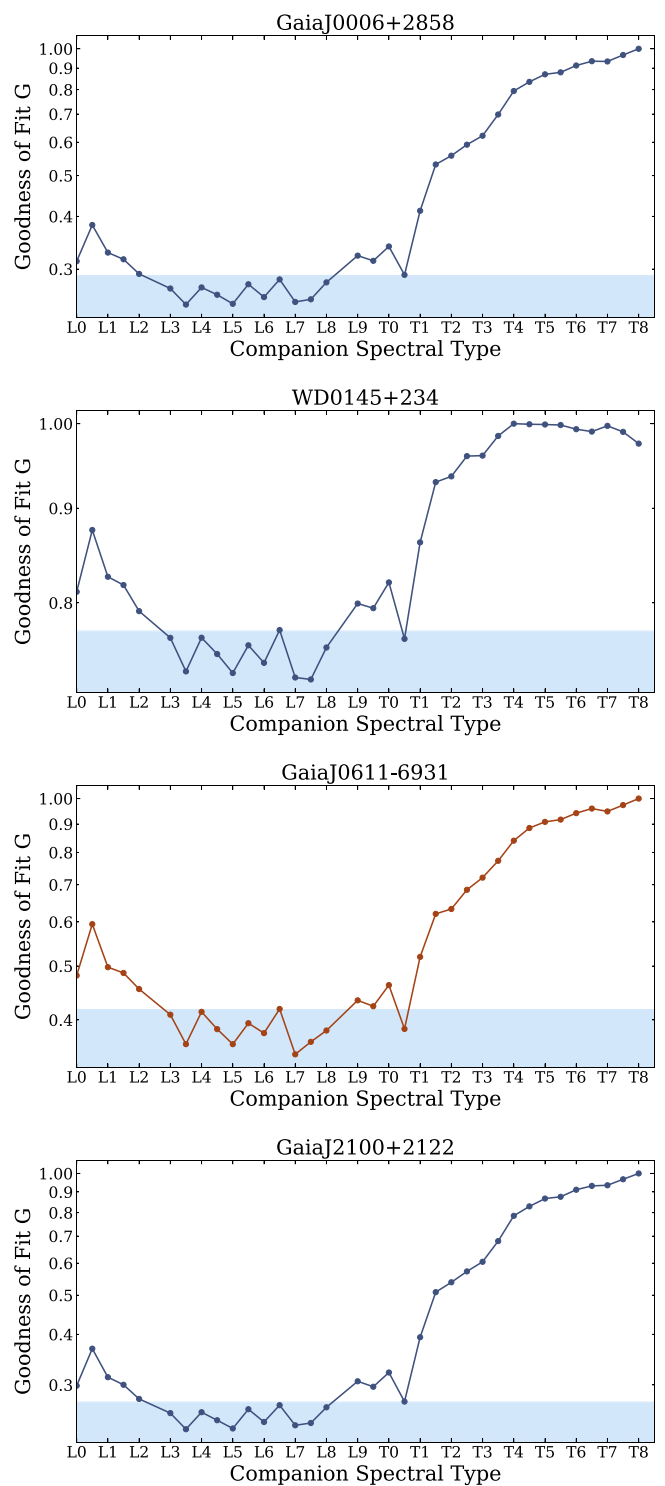

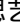










Figure A4. Similar to Figure A3, except for the four disk systems.

ORCID iDs

Dylan Owens  <https://orcid.org/0000-0002-6397-6719>
 Siyi Xu (许偲艺)  <https://orcid.org/0000-0002-8808-4282>
 Elena Manjavacas  <https://orcid.org/0000-0003-0192-6887>
 S. K. Leggett  <https://orcid.org/0000-0002-3681-2989>
 S. L. Casewell  <https://orcid.org/0000-0003-2478-0120>
 Erik Dennihy  <https://orcid.org/0000-0003-2852-268X>
 Patrick Dufour  <https://orcid.org/0000-0003-4609-4500>
 Beth L. Klein  <https://orcid.org/0000-0001-5854-675X>
 Sherry Yeh  <https://orcid.org/0000-0002-4037-3114>
 B. Zuckerman  <https://orcid.org/0000-0001-6809-3045>

References

- Allègre, C., Manhès, G., & Lewin, É. 2001, *E&PSL*, 185, 49
 Anders, F., Khalatyan, A., Queiroz, A. B. A., et al. 2022, *A&A*, 658, A91
 Astropy Collaboration, Price-Whelan, A. M., Lim, P. L., et al. 2022, *ApJ*, 935, 167
 Ballering, N. P., Levens, C. I., Su, K. Y. L., & Cleeves, L. I. 2022, *ApJ*, 939, 108
 Barber, S. D., Kilic, M., Brown, W. R., & Gianninas, A. 2014, *ApJ*, 786, 77
 Bear, E., & Soker, N. 2013, *NewA*, 19, 56
 Becklin, E. E., & Zuckerman, B. 1988, *Natur*, 336, 656
 Bochkarov, K. V., & Rafikov, R. R. 2011, *ApJ*, 741, 36
 Burgasser, A. J., Liu, M. C., Ireland, M. J., Cruz, K. L., & Dupuy, T. J. 2008, *ApJ*, 681, 579
 Casewell, S. L., Belardi, C., Parsons, S. G., et al. 2020, *MNRAS*, 497, 3571
 Casewell, S. L., Lawrie, K. A., Maxted, P. F. L., et al. 2015, *MNRAS*, 447, 3218
 Casewell, S. L., Littlefair, S. P., Parsons, S. G., et al. 2018, *MNRAS*, 481, 5216
 Chambers, K. C., Magnier, E. A., Metcalfe, N., et al. 2016, arXiv:1612.05560
 Chiu, K., Fan, X., Leggett, S. K., et al. 2006, *AJ*, 131, 2722
 Cruz, K. L., Burgasser, A. J., Reid, I. N., & Liebert, J. 2004, *ApJL*, 604, L61
 Cushing, M. C., Marley, M. S., Saumon, D., et al. 2008, *ApJ*, 678, 1372
 Cushing, M. C., Rayner, J. T., & Vacca, W. D. 2005, *ApJ*, 623, 1115
 Debes, J. H., Hoard, D. W., Wachter, S., Leisawitz, D. T., & Cohen, M. 2011, *ApJS*, 197, 38
 Dennihy, E., Xu, S., Lai, S., et al. 2020, *ApJ*, 905, 5
 Dufour, P., Bergeron, P., Liebert, J., et al. 2007, *ApJ*, 663, 1291
 Eikenberry, S. S., Elston, R., Raines, S. N., et al. 2004, *Proc. SPIE*, 5492, 1196
 Elias, J. H., Joyce, R. R., Liang, M., et al. 2006, *Proc. SPIE*, 6269, 62694C
 Foreman-Mackey, D., Hogg, D. W., Lang, D., & Goodman, J. 2013, *PASP*, 125, 306
 French, J. R., Casewell, S. L., Dupuy, T. J., et al. 2023, *MNRAS*, 519, 5008
 Gaia Collaboration, Vallenari, A., Brown, A. G. A., et al. 2022, arXiv:2208.00211
 Gänsicke, B. T., Marsh, T. R., Southworth, J., & Rebassa-Mansergas, A. 2006, *Sci*, 314, 1908
 Gentile Fusillo, N. P., Tremblay, P. E., Cukanovaite, E., et al. 2021, *MNRAS*, 508, 3877
 Girven, J., Gänsicke, B. T., Steeghs, D., & Koester, D. 2011, *MNRAS*, 417, 1210
 Hartmann, S., Nagel, T., Rauch, T., & Werner, K. 2011, *A&A*, 530, A7
 Hartmann, S., Nagel, T., Rauch, T., & Werner, K. 2016, *A&A*, 593, A67
 Jura, M. 2003, *ApJL*, 584, L91
 Jura, M. 2008, *AJ*, 135, 1785
 Jura, M., Farihi, J., Zuckerman, B., & Becklin, E. E. 2007, *AJ*, 133, 1927
 Kelson, D. D. 2003, *PASP*, 115, 688
 Kenyon, S. J., & Bromley, B. C. 2017a, *ApJ*, 850, 50
 Kenyon, S. J., & Bromley, B. C. 2017b, *ApJ*, 844, 116
 Kilic, M., Bergeron, P., Kosakowski, A., et al. 2020, *ApJ*, 898, 84
 Kilic, M., Farihi, J., Nitta, A., & Leggett, S. K. 2008, *AJ*, 136, 111
 Kirkpatrick, J. D., Barman, T. S., Burgasser, A. J., et al. 2006, *ApJ*, 639, 1120
 Klein, B., Jura, M., Koester, D., Zuckerman, B., & Melis, C. 2010, *ApJ*, 709, 950
 Lagos, F., Schreiber, M. R., Zorotovic, M., et al. 2021, *MNRAS*, 501, 676
 Lai, S., Dennihy, E., Xu, S., et al. 2021, *ApJ*, 920, 156
 Lew, B. W. P., Apai, D., Zhou, Y., et al. 2021, *AJ*, 163, 8
 Looper, D. L., Kirkpatrick, J. D., Cutri, R. M., et al. 2008, *ApJ*, 686, 528
 Manser, C. J., Gänsicke, B. T., Gentile Fusillo, N. P., et al. 2020, *MNRAS*, 493, 2127
 Maxted, P. F. L., Napiwotzki, R., Dobbie, P. D., & Burleigh, M. R. 2006, *Natur*, 442, 543
 McLean, I. S., McGovern, M. R., Burgasser, A. J., et al. 2003, *ApJ*, 596, 561
 McLean, I. S., Steidel, C. C., Epps, H., et al. 2010, *Proc. SPIE*, 7735, 77351E
 McLean, I. S., Steidel, C. C., Epps, H. W., et al. 2012, *Proc. SPIE*, 8446, 84460J
 Melis, C., Farihi, J., Dufour, P., et al. 2011, *ApJ*, 732, 90
 Melis, C., Jura, M., Albert, L., Klein, B., & Zuckerman, B. 2010, *ApJ*, 722, 1078
 Melis, C., Klein, B., Doyle, A. E., et al. 2020, *ApJ*, 905, 56
 Metzger, B. D., Rafikov, R. R., & Bochkarov, K. V. 2012, *MNRAS*, 423, 505
 Onken, C. A., Wolf, C., Bessell, M. S., et al. 2019, *PASA*, 36, e033
 Parsons, S. G., Hermes, J. J., Marsh, T. R., et al. 2017, *MNRAS*, 471, 976
 Prochaska, J. X., Hennawi, J., Cooke, R., et al. 2019, pypeit/PypeIt: Releasing for DOI, v0.11.0.1, Zenodo, doi:10.5281/zenodo.3506873
 Prochaska, J. X., Hennawi, J., Cooke, R., et al. 2020, pypeit/PypeIt: Release v1.0.0, Zenodo, doi:10.5281/zenodo.3743493
 Prochaska, J. X., Hennawi, J. F., Westfall, K. B., et al. 2020, *JOSS*, 5, 2308
 Rafikov, R. R. 2011a, *MNRAS*, 416, L55
 Rafikov, R. R. 2011b, *ApJL*, 732, L3
 Rafikov, R. R., & Garmilla, J. 2012, *ApJ*, 760, 123
 Reach, W. T., Kuchner, M. J., von Hippel, T., et al. 2005, *ApJL*, 635, L161
 Rebassa-Mansergas, A., Xu, S., Raddi, R., et al. 2022, *ApJL*, 927, L31
 Rocchetto, M., Farihi, J., Gänsicke, B. T., & Bergfors, C. 2015, *MNRAS*, 449, 574
 Rogers, L. K. 2023, *MNRAS*, submitted
 Sheppard, S. S., & Cushing, M. C. 2009, *AJ*, 137, 304
 Siegler, N., Close, L. M., Burgasser, A. J., et al. 2007, *AJ*, 133, 2320
 Steckloff, J. K., Debes, J., Steele, A., et al. 2021, *ApJL*, 913, L31
 Steele, P. R., Burleigh, M. R., Dobbie, P. D., et al. 2011, *MNRAS*, 416, 2768
 Steele, P. R., Saglia, R. P., Burleigh, M. R., et al. 2013, *MNRAS*, 429, 3492
 Van Hoof, P. A. M. 2018, *Galax*, 6, 63
 van Roestel, J., Kupfer, T., Bell, K. J., et al. 2021, *ApJL*, 919, L26
 Veras, D., Leinhardt, Z. M., Bonsor, A., & Gänsicke, B. T. 2014, *MNRAS*, 445, 2244
 Vogt, S. S., Allen, S. L., Bigelow, B. C., et al. 1994, *Proc. SPIE*, 2198, 362
 Wang, T.-g., Jiang, N., Ge, J., et al. 2019, *ApJL*, 886, L5
 Wilson, T. G., Farihi, J., Gänsicke, B. T., & Swan, A. 2019, *MNRAS*, 487, 133
 Xu, S., Dufour, P., Klein, B., et al. 2019, *AJ*, 158, 242
 Xu, S., & Jura, M. 2014, *ApJL*, 792, L39
 Xu, S., Jura, M., Dufour, P., & Zuckerman, B. 2016, *ApJL*, 816, L22
 Xu, S., Lai, S., & Dennihy, E. 2020, *ApJ*, 902, 127
 Zhang, Z. H., Pinfield, D. J., Gálvez-Ortiz, M. C., et al. 2017, *MNRAS*, 464, 3040
 Zhou, Y., Apai, D., Tan, X., et al. 2022, *AJ*, 163, 17